h*TR* and NHP2 independently activate DNA damage response at ALT telomeres

Maya Raghunandan[1], Dan Geelen[1], Eva Majerova [1,2] and Anabelle Decottignies[1*]

[1]: Genetic and Epigenetic Alterations of Genomes, de Duve Institute, Faculty of Pharmacy and Biomedical Sciences, Université catholique de Louvain, Brussels 1200, Belgium

[2]: Present Address: Hawaii Institute of Marine Biology, 46-007 Lilipuna Rd, Kaneohe, HI 96744, U.S.A

*Lead contact: anabelle.decottignies@uclouvain.be

Running title: h*TR* and NHP2 impact the ALT pathway

Abstract

About 10% of cancer cells employ the Alternative Lengthening of Telomeres (ALT) pathway instead of re-activating the h*TERT* subunit of telomerase. The h*TR* RNA subunit is also abnormally silenced in some ALT$^+$ cells not expressing h*TERT*, suggesting a possible negative impact of h*TR* on ALT, independently of telomerase. Accordingly, ectopically-expressed h*TR* reduces p-RPA^{S33} levels at ALT telomeres by promoting the hnRNPA1- and DNA-PK-dependent depletion of telomere-bound RPA. The resulting defective ATR signaling at telomeres impairs the recruitment of homologous recombination protein, RAD51. This induces ALT telomere fragility, increases POLD3-dependent C-circle production and promotes the recruitment of 53BP1 DNA damage marker at telomeres. In ALT$^+$ cells that naturally retain h*TR* expression, NHP2 H/ACA ribonucleoprotein levels are downregulated, likely to restrain DNA damage response (DDR) activation at telomeres through a reduced recruitment of 53BP1. This unexpected role of NHP2 is independent from h*TR*'s non-canonical function in modulating telomeric p-RPA^{S33}. Collectively, our study shines new light on the interference between telomerase- and ALT-pathways and unravels a crucial role for h*TR* and NHP2 in regulating DDR at ALT telomeres.

Keywords: ALT/ h*TR*/ NHP2/ telomerase/ RPA

Introduction

Telomeres are specialized ribonucleoprotein structures marking and protecting the ends of eukaryotic chromosomes. Human telomeric DNA sequences comprise 2 to 15 kb-long tracts of 5'-(*TTAGGG*)$_n$ double-stranded repeats, that culminate in a single-stranded 3' G-rich overhang. The telomeric terminus folds back to form a protective T-loop structure, reinforced in place by a multi-protein complex, the shelterin (O'Sullivan & Karlseder, 2010; Palm & de Lange, 2008). Shelterin-bound T-loops play crucial roles in preventing chromosome ends from activating ataxia telangiectasia mutated (ATM)-, or ataxia telangiectasia and Rad3 related (ATR)-dependent DNA damage response (DDR), thereby protecting cells from permanent cell cycle arrest or apoptosis (O'Sullivan & Karlseder, 2010; Sfeir & de Lange, 2012).

In normal somatic cells that lack an active telomere maintenance mechanism (TMM), telomeres progressively shorten with cell divisions. Erosion ultimately culminates into telomere uncapping and subsequent exposure of chromosome ends to the DDR machinery, driving the cells to an irreversible state of senescence (Blackburn, 1991; Roake & Artandi, 2020; Martínez & Blasco, 2015). Cancer cells circumvent entry into senescence and attain immortality by maintaining their telomere length via one of two, mutually exclusive, TMMs: 1) reactivation of the h*TERT* gene encoding the catalytic subunit of telomerase (TEL^+ cells) or 2) hijacking a subset of cellular DNA replication and repair factors to perform Alternative Lengthening of Telomeres (ALT^+ cells) (Cesare & Reddel, 2010; Shay & Wright, 2005). While 80-85% of cancer cells rely on telomerase activity, an estimated 10% of cancers use the ALT mechanism and its frequency may reach up to 20% in pediatric cancers (Shay & Bacchetti, 1997; Heaphy *et al*, 2011; Claude & Decottignies, 2020).

The telomerase complex comprises two main subunits: hTERT, the reverse transcriptase component, and h*TR*, the RNA subunit that serves as template for reverse transcription (Greider & Blackburn, 1985; Nandakumar & Cech, 2013). The h*TR* RNA contains an H/ACA motif that binds four chaperone proteins – Dyskerin (DKC1), GAR1, NHP2 and NOP10 – for subsequent association with the hTERT subunit and formation of a functional telomerase holoenzyme complex (Wang & Meier, 2004; Tseng *et al*, 2015). In ALT^+ cells, telomeric DNA synthesis relies on inter- and intra- chromosomal recombination events. Specifically, ALT^+ cells use a specialized form of homologous recombination (HR), which closely resembles the conservative, RAD52-mediated break induced replication (BIR) process in yeast, and is prevalent in post-replicative, mitotic phase of the cell cycle (Sobinoff & Pickett, 2020; Min

et al, 2017; Teng *et al*, 2000; Dunham *et al*, 2000; Dilley *et al*, 2016). ALT$^+$ cells are characterized by several phenotypical markers, such as highly heterogeneous telomere length, reduced nucleosome density, increased abundance of partially single-stranded extrachromosomal C-rich telomeric DNA circles (C-circles), increased telomeric sister chromatid exchanges and the presence of ALT-associated PML bodies (APBs) (Dilley & Greenberg, 2015; Episkopou *et al*, 2014; Henson *et al*, 2009; Yeager *et al*, 1999). Enriched particularly in the G2 phase of the cell cycle, APBs facilitate the clustering of telomeres within PML bodies and provide a recombinogenic microenvironment containing several known DNA repair and recombination proteins, including RPA, RAD51, RAD52, BLM, FANCD2 and FANCM, to name a few (Cho *et al*, 2014; Grudic *et al*, 2007; Pan *et al*, 2017; Root *et al*, 2016). ALT DNA synthesis, in fact, occurs largely within the APBs (Zhang *et al*, 2019a), with PML-mediated recruitment of the BLM–TOP3A–RMI (BTR) complex to ALT telomere ends being a key step (Loe *et al*, 2020).

From the first discovery of human ALT$^+$ cells in the late nineties, it appeared that, in addition to the failure in re-activating h*TERT* gene expression, ALT$^+$ cells frequently lacked h*TR* RNA expression (Bryan *et al*, 1997). In contrast, somatic cells constitutively express h*TR* (Takakura *et al*, 1998; Cong *et al*, 2002), raising the possibility that losing h*TR* expression, even in the absence of h*TERT,* may be advantageous in ALT$^+$ cells. A previous study suggested that h*TR*, through rather poorly understood non-canonical functions, restrains ATR kinase activity following UV-induced replication stress (Kedde *et al*, 2006). As ALT$^+$ cells display hypersensitivity to ATR inhibitors (Flynn *et al*, 2015), this non-canonical function of h*TR* alluded to a possible explanation as to why h*TR* expression may be deleterious to these cells. Alternatively, h*TR* may be deleterious to ALT$^+$ cells through its ability to activate the DNA-PK-dependent phosphorylation of hnRNPA1 (Ting *et al*, 2005; Ting *et al*, 2009; Le *et al*, 2013), a process known to promote the removal of RPA protein from telomeres (Flynn *et al*, 2011; Sui *et al*, 2015). Canonical functions of h*TR*, on the other hand, represent an added insult to ALT$^+$ cells as telomerase activity and ALT likely repress each other at telomeres (Claude & Decottignies, 2020).

Here, we took advantage of a robust model system of cellular hybrids to investigate whether and how ALT$^+$ hybrids can repress the expression of telomerase subunits, inherited from the TEL$^+$ parental cells during the hybridization procedure. We found that, in one hybrid, telomerase activity was repressed through h*TR* gene silencing. In another hybrid however, telomerase activity was repressed despite retaining both h*TERT* and h*TR* expression. We further show that, independently of telomerase activity, h*TR* expression in ALT$^+$ cells

downregulates the abundance of both phosphorylated RPA (p-RPA^{S33}) and the HR protein-RAD51 at telomeres. Consequently, h*TR*-expressing ALT$^+$ cells displayed increased telomere fragility, likely due to persistently stalled replication forks, along with an increased recruitment of 53BP1 at telomeres and an exacerbated POLD3-dependent formation of C-circles. We report that this non-canonical function of h*TR* in downregulating telomere-associated p-RPA^{S33} relies on its previously reported connection with DNA-PK (Ting *et al*, 2005) and the DNA-PK/hnRNPA1 axis of telomere regulation (Ting *et al*, 2009; Flynn *et al*, 2011; Le *et al*, 2013; Sui *et al*, 2015). We also unraveled an intriguing inverse correlation between h*TR* and NHP2 protein expression in ALT$^+$ cells and propose that NHP2 downregulation in h*TR*-expressing ALT$^+$ cells acts as an adaptive mechanism to downregulate 53BP1-mediated DNA damage response at telomeres, independently of h*TR*. Finally, while ALT$^+$ cells preferentially downregulate h*TR*, they still continue to depend on very low levels of h*TR* to stay protected from cell death, as was shown previously for CD4$^+$ T-cells in the context of yet another, but poorly understood non-canonical function of h*TR* (Gazzaniga & Blackburn, 2014).

Results

Downregulation of telomerase activity in ALT$^+$ hybrid cells

Hybridization between TEL$^+$ and ALT$^+$ cells generates unstable hybrids that need to repress one of the two original TMMs inherited from the parental cells to exclusively maintain a singular active mechanism (Bower *et al*, 2012; Episkopou *et al*, 2014, 2019). We previously fused two IMR90 fetal lung fibroblast-derived, immortalized, post-crisis survivors: SW39/TEL$^+$ and IMRB/ALT$^+$. Through two independent hybridization procedures, we generated numerous hybrids, including SI14/TEL$^+$ (1st hyb), 6C3/TEL$^+$ (2nd hyb), SI24/ALT$^+$ (1st hyb) and 8G12/ALT$^+$ (2nd hyb). Both SI24/ALT$^+$ and 8G12/ALT$^+$ clones lacked ATRX expression and displayed increased APBs, together with heterogeneous telomere length profiles (Episkopou *et al*, 2019). Agreeing with the mutual exclusion of the two TMMs, although all hybrids initially express an active telomerase complex, stable ALT$^+$ hybrids showed no (SI24/ALT$^+$) or barely detectable (8G12/ALT$^+$) telomerase activity, *in vitro*, as determined using the ddTRAP assay (Ludlow *et al*, 2018) (Fig 1A). To determine the mechanism of telomerase repression, we measured h*TR* and h*TERT* mRNA expression. In SI24/ALT$^+$ hybrids, h*TR* levels were very low and comparable to IMRB/ALT$^+$ parental cells, while h*TERT* mRNA levels were similar to those detected in the TEL$^+$ hybrids and the SW39/TEL$^+$ parental cells (Fig 1B). In 8G12/ALT$^+$ hybrids however, h*TR*

expression was only reduced to about 50% of SW39/TEL$^+$ levels (Fig 1B). In SI24/ALT$^+$ hybrid, we found that h*TR* repression occurred progressively: immediately after hybrid selection (PD 0), h*TR* levels were in fact, similar to those detected in TEL$^+$ hybrids and, at PD 76, 18% of h*TR* levels were still present (Fig 1B).

To determine if the observed h*TR* level reduction in SI24/ALT$^+$ hybrid resulted from transcriptional silencing, first, we examined the binding of RNA polymerase II (RNA Pol II) to the h*TR* promoter. Compared to SI14/TEL$^+$, SI24/ALT$^+$ cells showed a significantly reduced binding of RNA Pol II to h*TR* promoter (Fig 1C, $p<0.0001$). In stark contrast, RNA Pol II binding at h*TR* promoter of 8G12/ALT$^+$ cells was at par with that observed in SI14/TEL$^+$ (Fig 1C). We then asked if excessive heterochromatinization of the h*TR* promoter – marked by posttranslational modifications (PTMs) of histone H3 – could account for the reduced RNA Pol II binding in SI24/ALT$^+$ cells, but we did not detect any increase in H3K9me3 or H3K27me3 repressive marks, compared to SI14/TEL$^+$ cells (Fig 1D). Simultaneously, we observed a strong reduction in H3 PTMs that mark active transcription: H3Ac and H3K4me3 (Fig 1D, $p=0.003$, $p=0.00001$, respectively). The reduced transcription from h*TR* promoter in SI24/ALT$^+$ cells is further supported by a reduction in NFYB binding, a transcription-activating factor for h*TR* (Zhao *et al*, 2005) (Fig 1E, $p=0.002$). To confirm that NFYB binding is a reliable indicator of h*TR* transcription, we verified that NFYB binding at the h*TR* promoter of IMRB/ALT$^+$ parental cells – with known hypermethylation of DNA – is significantly lower than SW39/TEL$^+$ cells (Fig 1E, $p=0.009$).

Collectively, these findings demonstrate that, in SI24/ALT$^+$ cells, transcription from the h*TR* promoter is actively suppressed, independently of promoter heterochromatinization. Conversely, in 8G12/ALT$^+$ cells, even though telomerase activity is almost completely repressed and h*TR* expression levels are reduced, transcription from the h*TR* promoter does not seem to be downregulated, suggesting that each ALT$^+$ hybrid has adopted a distinct mechanism for suppressing telomerase activity.

The H/ACA box ribonucleoprotein NHP2 protein levels are downregulated in h*TR* expressing-8G12/ALT$^+$ cells

To understand why 8G12/ALT$^+$ cells – which retain h*TERT* mRNA expression, along with significant h*TR* transcript levels – exhibit barely detectable telomerase activity *in vitro*, we examined the steady-state levels of proteins that associate with h*TR* to facilitate the formation of

a functional hTERT-h*TR* holoenzyme complex and are known to stabilize the RNA subunit: NHP2, NOP10, GAR1 and DKC1 (Fu & Collins, 2006, 2007; MacNeil *et al*, 2016). While the tested TEL$^+$ and ALT$^+$ hybrids show comparable protein levels for NOP10, GAR1 and DKC1, the steady-state levels of NHP2 protein are reduced by about 60% in 8G12/ALT$^+$ cells, in comparison to SI14/TEL$^+$ (Fig 2A, p<0.0001). As the reduced NHP2 protein levels in 8G12/ALT$^+$ cells are not associated with *NHP2* mRNA downregulation (Fig 2B), we next sought to determine whether NHP2 protein might be susceptible to proteasomal degradation in 8G12/ALT$^+$ cells. Treatment of 8G12/ALT$^+$, SI24/ALT$^+$ and SI14/TEL$^+$ cells with MG132 proteasome inhibitor revealed that the NHP2 protein undergoes proteasomal degradation in all three cell lines (Fig 2C). Our results further indicate that the MG132 treatment may not fully erase the differences between 8G12/ALT$^+$ and the other cell lines, suggesting that additional post-transcriptional regulatory mechanisms may account for the reduced NHP2 protein levels in 8G12/ALT$^+$ cells (Fig 2C).

NHP2 downregulation was previously reported to reduce both h*TR* levels and *in vitro* telomerase activity (Benyelles *et al*, 2020; Vulliamy *et al*, 2008). To evaluate the impact of NHP2 on these two parameters in the hybrid cells, we transiently depleted NHP2 with siRNAs in 6C3/TEL$^+$ and SI14/TEL$^+$ cell lines. h*TR* levels were reduced by about 2-fold and telomerase activity, assayed by ddTRAP, was reduced to 10-40% of their respective control levels (Supplementary Fig S1A and B). To test whether the downregulation of NHP2 protein in 8G12/ALT$^+$ cells may be responsible for the drastic reduction of telomerase activity, we ectopically and transiently overexpressed NHP2 in 8G12/ALT$^+$ cells using a lentiviral NHP2-IRES-GFP plasmid. FACS analysis showed a 98% content of GFP-positive cells, with about 200-fold more NHP2 expression than in parental 8G12/ALT$^+$ cells (Fig 2D). Strikingly however, NHP2 overexpression alone was insufficient to rescue telomerase activity in these cells (Fig 2E), suggesting that the downregulation of NHP2 in 8G12/ALT$^+$ cells is unrelated to telomerase activity inhibition. While the mechanisms underlying telomerase activity repression in 8G12/ALT$^+$ cells remain unknown, this observation led us to hypothesize that NHP2 protein downregulation may be advantageous to 8G12/ALT$^+$ cells, in a telomerase-independent manner. Hence, we anticipated that NHP2-overexpressing 8G12/ALT$^+$ cells may experience adaptation mechanisms to cope with the simultaneous robust expressions of both NHP2 and h*TR*. In line with this hypothesis, upon examining two stable clonal populations of 8G12/ALT$^+$ cells overexpressing NHP2, 8G12/ALT$^+$+NHP2$^{\#2}$ and 8G12/ALT$^+$+NHP2$^{\#3}$ (Fig 2F), we found that, compared to 8G12/ALT$^+$ cells, both clones had strongly repressed h*TR* expression, by 99.8% and 97% respectively (Fig 2G) and, as expected, telomerase activity was still repressed

(Supplementary Fig S1C). Subsequently, RNA Pol II ChIP experiments revealed a significantly reduced binding efficiency of RNA Pol II at the h*TR* promoter of both 8G12/ALT$^+$+NHP2$^{\#2}$ and 8G12/ALT$^+$+NHP2$^{\#3}$ cells (Fig 2H, p=0.001), suggesting that the stable ectopic overexpression of NHP2 in 8G12/ALT$^+$ cells leads to its transcriptional repression. Importantly, h*TR* expression was not lost in NHP2-overexpressing SI14/TEL$^+$+NHP2$^{\#6}$ cells used as controls (Fig 2F and G).

These findings raise an interesting hypothesis that, in 8G12/ALT$^+$ cells, high NHP2 expression levels are incompatible with h*TR* expression, and this, independently of telomerase activity regulation.

h*TR*-expressing ALT$^+$ cancer cell lines consistently display reduced NHP2 protein levels

To determine if the inverse correlation between h*TR* and NHP2 protein levels that we observed in 8G12/ALT$^+$ cells could be a general telomerase-independent phenomenon in ALT$^+$ cells, we sought to compare NHP2 protein levels in additional available ALT$^+$ cell lines that do not express h*TERT* but have naturally either retained or silenced h*TR* expression. U2OS/ALT$^+$ (osteosarcoma), SaOS-2/ALT$^+$ (osteosarcoma) and VA13/ALT$^+$ (SV40T-immortalized fetal lung fibroblasts) are well-characterized ALT$^+$ cell lines; LB188/ALT$^+$ (rhabdomyosarcoma) (Tilman *et al*, 2009) and LB857/ALT$^+$ (myxoid sarcoma) cell lines were established in-house from resected tumors. The presence of ALT activity in the latter two cell lines was confirmed and contrasted with LB23/TEL$^+$ (rhabdomyosarcoma, established in-house) cells for lack of telomerase activity, telomere length heterogeneity, C-circles and APB formation (Supplementary Fig S2A, B, C and D). As expected, all ALT$^+$ cell lines express barely detectable h*TERT* mRNA when compared to the LB23/TEL$^+$ cells or the commercially available 143B/TEL$^+$ osteosarcoma cell line used as reference (Fig 3A). As for the h*TR* subunit, expression levels ranged from low to high in SaOS-2/ALT$^+$, LB857/ALT$^+$ and LB188/ALT$^+$ cell lines but were barely detectable in U2OS/ALT$^+$ and VA13/ALT$^+$ (Fig 3A). These cell lines were thus classified as either ALT$^+$/hTR$^+$ (LB857, LB188, SaOS-2) or ALT$^+$/hTR$^-$ (U2OS, VA13). While all five ALT$^+$ cell lines exhibit varying levels of *NHP2* mRNA expression, with no discernible pattern or trend (Fig 3A), we found an inverse correlation between NHP2 protein levels and h*TR* expression: SaOS-2, LB857 and LB188 ALT$^+$/hTR$^+$ cancer cells express significantly lower levels of NHP2 protein compared to U2OS and VA13 ALT$^+$/hTR$^-$ cells (Fig 3B, p=0.0003).

Together with our findings in 8G12/ALT$^+$ cells that NHP2 overexpression silences h*TR*, these anti-correlations in additional ALT$^+$ cell lines further suggest that ALT$^+$ cells may adapt to the presence of h*TR* by downregulating NHP2 protein levels. Furthermore, our observations strongly suggest that h*TR* expression may somehow impair ALT$^+$ cell fitness.

Ectopic expression of h*TR* in ALT$^+$/hTR$^-$/hTERT$^-$ cells downregulates p-RPA^{S33} abundance at telomeres

Our observations led us to investigate whether h*TR* may indeed impair ALT activity independently of telomerase. First, in line with the previously reported ability of h*TR* to suppress ATR kinase activity in response to DNA damage (Kedde *et al*, 2006), and knowing that ALT$^+$ cells are hypersensitive to ATR inhibitors (Flynn *et al*, 2015), we hypothesized that h*TR* expression in ALT$^+$ cells could potentially downregulate ATR activity. Possibly, NHP2 could further aid and facilitate h*TR*'s non-canonical function as a negative regulator of ATR kinase.

To test this, we ectopically overexpressed h*TR* in two distinct ALT$^+$/hTR$^-$/hTERT$^-$ cell lines: the U2OS/ALT$^+$ osteosarcoma cell line and the IMRB/ALT$^+$ SV40T-transformed fibroblast cell line (Fig 4A) (these ALT$^+$ cell lines will be referred to as U2OS and IMRB, *hitherto*, for simplicity). Right after establishing stable h*TR* transfection in the two cell lines, we saw no change in NHP2 protein levels (Fig 4B), allowing us to directly test the impact of h*TR* expression on ATR activity at ALT telomeres. Supporting the mutual exclusion of h*TR* and NHP2 in long-term cultures however, we did observe a downregulation of NHP2 protein expression in some IMRB-hTR clones following extensive passaging (Supplementary Fig S3A and B). h*TR*-expressing U2OS and IMRB ALT$^+$ cells showed a slight, but significant, reduction in cellular growth rate (Fig 4C, p=0.01) in the absence of noticeable difference in telomeric DNA content (Supplementary Fig S3C). To assess whether h*TR* overexpression may impact global ATR activity in either untreated or hydroxyurea (HU)-treated U2OS cells, we performed western blot analyses of CHK1-S345 phosphorylation (p-CHK1^{S345}), a direct target of ATR, and of ATR-T1989 auto-phosphorylation site (p-ATR^{T1989}). This analysis however did not reveal any difference between U2OS and U2OS-hTR cells, either at basal level or after treatment with HU (Fig 4D). On the other hand, the western blots revealed small reductions in the total levels of RPA^{S33} phosphorylation (p-RPA^{S33}), another ATR target site (Olson *et al*, 2006; Silva *et al*, 2019), in both untreated and HU-treated h*TR*-expressing cells compared to the U2OS parental cell line (Fig 4D).

ALT$^+$ cells are characterized by the accumulation of RPA at single-stranded telomeric DNA outside S phase and the protein gets phosphorylated by ATR on S33, likely at sites of residual DNA replication fork stalling (Grudic *et al*, 2007; Olson *et al*, 2006; Silva *et al*, 2019). To determine whether the reduction in total p-RPA^{S33} signals that we observed by western blots might specifically arise from telomeres, we performed IF/FISH experiments. Accordingly, we detected significantly reduced p-RPA^{S33} co-localizations with ALT$^+$ telomeres upon h*TR* overexpression in both U2OS and IMRB cell lines (Fig 4E, p<0.0005 and p=0.002 respectively). Treatment with VE-821 ATR inhibitor confirmed that the observed p-RPA^{S33} IF signals are indeed ATR-dependent (Supplementary Fig S4A). Importantly, RPA^{S33} phosphorylation was not detected in TEL$^+$ cell extracts (Supplementary Fig S4B), further supporting that the observed p-RPA^{S33} signal in cellular extracts emanates from ALT telomeres.

If h*TR* overexpression reduces p-RPA^{S33} levels, we expected h*TR* depletion to increase them. Previously, h*TR* depletion in CD4$^+$ T cells was associated with massive cell death in response to apoptosis (Gazzaniga & Blackburn, 2014). We similarly observed massive cell death following 3 days of h*TR* depletion in both TEL$^+$ and ALT$^+$ cells, regardless of the h*TR* expression levels (Fig 4F). As the pre-apoptotic cells do not display any increase in p-CHK1^{S345} levels (Fig 4G), the cell death appears to occur independently of ATR hyper-activation. Notably, in line with our observation that h*TR* expression modulates p-RPA^{S33} levels in ALT$^+$ cells, we detected higher levels of RPA^{S33} phosphorylation only in h*TR*-depleted ALT$^+$ cells, and not in TEL$^+$ cells (Fig 4G).

The above data suggest that h*TR* overexpression in ALT$^+$ cells reduces p-RPA^{S33} signals at telomeres, without globally repressing ATR activity. Simultaneously, and through still undefined telomerase-independent mechanisms, we confirm that h*TR* is required for cell viability, even in ALT$^+$ cells that display barely detectable h*TR* levels.

Ectopic expression of h*TR* in ALT$^+$/hTR$^-$/hTERT$^-$ cells exacerbates telomeric damages and C-circle formation

Next, we investigated the consequences of reduced telomeric p-RPA^{S33} levels in ALT$^+$ cells with ectopic h*TR* expression. Telomeres are known hot spots for replication stress and represent common fragile sites within the genome (Verdun & Karlseder, 2006; Sfeir *et al*, 2009). ALT telomeres, furthermore, with the increased incidence of telomeric R-loops, harbor persistent DNA damage as a consequence of increased replication fork stalling (Sobinoff &

Pickett, 2017; Cesare *et al*, 2009; Cesare & Reddel, 2010; Cox *et al*, 2016). Typically, ATR kinase, through a signaling cascade initiated by its ssDNA-RPA complex-dependent recruitment to stalled sites (Kidiyoor *et al*, 2016), facilitates restart of the replication forks. This involves a complex series of molecular events, in which phosphorylation of RPA^{S33} plays a major role, to resume DNA synthesis through fork reversal and recombination, without chromosomal breakage (Toledo *et al*, 2013; Neelsen *et al*, 2013). Consequently, disrupting ATR signaling increases telomere fragility (Kedde *et al*, 2006; McNees *et al*, 2010; Sfeir *et al*, 2009; Mokrani-Benhelli *et al*, 2013; Pennarun *et al,* 2010).

Hence, we next asked whether U2OS-hTR cells display increased telomere fragility – either in the G-rich lagging telomeric strand or the C-rich leading telomeric strand – using the telomere chromosome-orientation FISH (CO-FISH) assay. Accordingly, compared to U2OS cells, U2OS-hTR cells showed a distinct increase in fragile telomeres marked by a "smeary or doublet signal" on both leading and lagging strands (Fig 5A, p=0.0007 and p=0.0004, respectively). Further validating the reduced ATR signaling at telomeres of these cells was the observation that RAD51 recruitment, an ATR-dependent process (Buisson *et al*, 2017), was significantly downregulated at telomeres of h*TR*-expressing U2OS or IMRB cells (Fig 5B, p<0.0001 and p=0.0008 respectively).

A defective ATR signaling at stalled replication forks can lead to fork collapse (Couch *et al*, 2013; Mutreja *et al*, 2018), resulting in DNA double-strand breaks marked by the recruitment of 53BP1. When happening at telomeres, collapsed replication forks give rise to Telomere dysfunction-Induced Foci or TIF. To test whether h*TR*-expressing ALT^+ cells experience more fork collapses at telomeres, we monitored 53BP1 recruitment at telomeres of U2OS, U2OS-hTR, IMRB and IMRB-hTR cells. We detected a significant increase of TIF in h*TR*-expressing cells compared to their respective parental counterparts (Fig 5C, p<0.0001). Interestingly, ATR inhibitor treatment did not further increase TIF abundance in U2OS-hTR cells (Fig 5D and E), suggesting that the h*TR*-dependent impact on telomere dysfunction is epistatic with ATR inhibition. On the other hand, and as expected, treatment with KU5593 ATM kinase inhibitor (ATMi), which blocks 53BP1-mediated DSB repair, abrogated TIF in both U2OS and U2OS-hTR cells (Fig 5D and E).

In light of recent studies showing that aberrant fork reversal increases POLD3 recruitment at telomeres and C-circle formation (Silva *et al*, 2019; Lu *et al*, 2019), we hypothesized that h*TR*-expressing ALT^+ cells may similarly produce more POLD3-dependent C-circles. Accordingly, we found that, compared to their respective parental cells, U2OS-hTR and

IMRB-hTR cells, both showed a significant increase in POLD3 recruitment at telomeres (Fig 5F, $p<0.0001$), along with a significantly higher production of POLD3-dependent production of C-circles (Fig 5G, H and I). Agreeing with our observation that h*TR*-expressing ALT$^+$ cells do not globally repress ATR activity, and in line with the previous demonstration that ATR activity is required for efficient C-circle production (Flynn *et al*, 2015; Zhang *et al*, 2019b), we found that ATR depletion still reduces C-circle production in U2OS-hTR cells (Supplementary Fig S5).

Together, these data show that h*TR* expression induces telomere fragility in ALT$^+$ cells, leading to an increased POLD3-dependent production of C-circles.

More APBs are actively engaged in G2/M telomeric DNA synthesis in ALT$^+$ cells ectopically expressing h*TR*

POLD3-mediated C-circle generation occurs primarily within APBs (Zhang *et al*, 2019a). Our observation that POLD3-dependent C-circle formation is upregulated in h*TR*-overexpressing ALT$^+$ cells led us to check whether the upregulated C-circle production may be a consequence of increased abundance of APBs. However, both U2OS-hTR and IMRB-hTR cells showed a significant reduction in the total number of PML bodies, and consequently, in APB formation, when compared to U2OS and IMRB cells, respectively (Fig 6A, $p<0.0001$). To resolve this conundrum, we monitored the G2/M telomeric DNA synthesis in U2OS-hTR cells using the previously described ATSA assay (ALT telomere DNA synthesis in APBs) (Zhang *et al*, 2019a) (Fig 6B). Cells were first synchronized using thymidine, then arrested in G2/M-phase with the RO-3306 CDK1 inhibitor and ultimately released into medium containing the thymidine analog 5-Ethynyl-2′-deoxyuridine (EdU) for 1 h. In these cells, EdU detection, combined with PML-IF and telomeric FISH was used to visualize newly synthesized telomeric DNA within the APBs (Fig 6C and D). We found that, even though U2OS-hTR cells show a reduced APB content, the percentage of APBs actively engaged in G2/M telomeric DNA synthesis is significantly higher compared to parental U2OS cells (Fig 6E, $p<0.0001$). This finding suggests that an increased proportion of APBs within every nucleus is actively engaged in G2/M telomeric DNA synthesis in U2OS-hTR cells.

The reduced abundance of PML bodies in h*TR*-expressing ALT$^+$ cells is still unexplained but likely involves post-transcriptional regulations, as we found no corresponding reduction in *PML* mRNA levels in these cells (Supplementary Fig S6). We anticipate that this may be related to the still undefined non-canonical function of h*TR* in protecting cells against apoptosis

(Gazzaniga & Blackburn, 2014) as PML bodies play important roles in apoptosis regulation (Hsu & Kao, 2018).

h*TR* overexpression induces a DNA-PK and hnRNPA1-dependent depletion of RPA from ALT telomeres

h*TR* expression in ALT$^+$ cells appears to specifically reduce telomeric p-RPA^{S33} levels. As ATR kinase activity is not globally repressed by h*TR*, we hypothesized that the reduced abundance of telomeric p-RPA^{S33} may be linked to a reduced abundance of telomere-bound RPA. As the total cellular RPA protein levels do not appear to be downregulated by h*TR* (Fig 4D), the impact may be telomere-specific. To address this possibility, we combined native FISH with IF against RPA, since RPA binds to single-stranded DNA (Fig 7A). To avoid any bias due to distinct cell cycle distribution and to account for the G2/M synthesis of telomeres in ALT$^+$ cells, we performed the experiment in G2/M synchronized cells. Although both C-rich (Fig 7B, p=0.01) and G-rich (Supplementary Fig S7A, p<0.0001) native FISH signals were increased in h*TR*-expressing cells and – likely reflecting the replication stress at those telomeres – we found a significant 1.5-fold downregulation of RPA foci abundance in U2OS-hTR cells (Fig 7B, p<0.0001). Consequently, the C-rich native FISH signals associated with RPA foci dropped from 94% of the total ss-telomeric DNA signals in U2OS cells to 70% in U2OS-hTR cells (Fig 7C, p<0.0001). Together, these data indicate that RPA is depleted from ss-telomeric DNA in U2OS-hTR cells.

Previously, h*TR* was reported to directly interact with the KU80 subunits of DNA-PK complex (Ting *et al*, 2005) and this interaction was further shown to promote the DNA-PK-dependent phosphorylation of hnRNPA1, another protein of the h*TR*/DNA-PK complex (Ting *et al*, 2009; Le *et al*, 2013). In turn, phosphorylated hnRNPA1 was reported to facilitate the removal of RPA from telomeres after S phase (Sui *et al*, 2015), a process first reported by Flynn *et al.* and involving the TERRA telomeric non-coding RNA (Flynn *et al*, 2011). We therefore reasoned that h*TR* overexpression in ALT$^+$ cells may promote the DNA-PK and hnRNPA1-dependent removal of RPA from ALT telomeres. To address this hypothesis, we first depleted hnRNPA1 from U2OS-hTR cells and evaluated telomeric RPA foci abundance. We found that the hnRNPA1 knock-down rescues the telomeric RPA foci of U2OS-hTR cells and that this, in turn, rescues telomeric p-RPA^{S33} levels (Fig 7D and E, p=0.02 and p=0.002, respectively). Simultaneously, we also observed comparable rescue of telomere-bound RPA in U2OS-hTR

cells following treatment with the DNA-PKcs inhibitor Nu7026 (Fig 7F, *p*=0.004). Unexpectedly however, hnRNPA1 depletion, as well as DNA-PKcs inhibitor treatment had an opposite impact on telomeric RPA foci in U2OS cells and reduced their abundance (Fig 7D, E and F, p<0.0001 and p=0.0002 respectively). This raises an interesting hypothesis that h*TR* might be required in ALT^+ cells to establish the hnRNPA1-dependent removal of RPA from telomeres, a phenomenon initially reported in HeLa/TEL^+ cells (Flynn *et al*, 2011). Why hnRNPA1 depletion or DNA-PKcs inhibition depletes RPA from telomeres of U2OS cells that do not express h*TR* is still unsolved but suggests an opposite role for the DNA-PK/hnRNPA1 complex in keeping RPA at telomeres of cells that do not express h*TR*. Hence, we speculate that h*TR* may switch DNA-PK/hnRNPA1 from an RPA-maintaining to an RPA-removing complex at telomeres.

Altogether, our results suggest that h*TR* promotes the DNA-PK- and hnRNPA1-dependent removal of RPA complex from ALT telomeres, likely through its previously reported interaction with the KU subunits of DNA-PK.

NHP2 downregulation reduces telomeric dysfunction independently of h*TR*'s impact on telomeric p-RPA^{S33} levels

At this stage, our results provided some explanations as to why h*TR* silencing is beneficial to ALT^+ cells. Our observation that the ALT^+ cell lines that retain h*TR* expression appear to downregulate NHP2 protein levels (Fig 2 and 3) was however still unexplored. As NHP2 is a well-known chaperone of h*TR* for its canonical function as telomerase subunit (Wang & Meier, 2004; Tseng *et al*, 2015), we first hypothesized that reducing NHP2 protein levels may similarly impair h*TR*'s non-canonical function of reducing telomeric p-RPA^{S33} levels at ALT^+ telomeres. To address this, we depleted NHP2 from U2OS-hTR cells and monitored telomeric p-RPA^{S33} foci. First, we verified that the residual h*TR* levels of NHP2-depleted U2OS-hTR cells, while reduced compared to U2OS siLuc, were still comparable to SI14/TEL^+ cells (Fig 8A). As NHP2 depletion did not alleviate the h*TR*-mediated downregulation of telomeric p-RPA^{S33} (Fig 8B and C, *p*=0.37), we concluded that the chaperone is not required for this non-canonical function of h*TR*.

Our results therefore suggested that the NHP2 protein may be deleterious to h*TR*-expressing ALT^+ cells through a mechanism not involving its chaperoning activity towards h*TR.* H/ACA ribonucleoproteins, including NHP2, have been reported to promote the accumulation of DNA damage biomarkers in response to genotoxic stress, although the underlying mechanisms

are still unknown (Lin *et al*, 2015). As newly-established h*TR*-expressing ALT$^+$ cells show an increased incidence of 53BP1 foci at telomeres (Fig 5C), we asked whether NHP2 downregulation may contribute to ALT$^+$ cell fitness by reducing 53BP1-mediated DNA damage signaling. Accordingly, we found that NHP2 depletion largely reduced the differences in TIF frequency between U2OS and U2OS-hTR cells (Fig 8D), in the absence of any detectable downregulation of 53BP1 protein levels (Fig 8E). Reduction in 53BP1 foci was not specific to telomeres as we found a corresponding decrease of non-telomeric 53BP1 foci abundance (Supplementary Fig S8A). Furthermore, the increased incidence of TIF following treatment with DSB-inducing agent doxorubicin (DOXO) in both U2OS siLuc and U2OS-hTR siLuc cells, was significantly reduced in the corresponding siNHP2-treated cells (Fig 8D, p<0.0001). The impact of NHP2 knock-down on 53BP1 foci and TIF was also observed in the SaOS-2/ALT$^+$ cells, that naturally express h*TR,* and in doxorubicin-treated 143B/TEL$^+$ osteosarcoma cells (Supplementary Fig S8B, C, D and E), suggesting a general role of NHP2 in the DDR pathway.

Supporting a role for NHP2 in 53BP1 recruitment at DSBs, we found that, following exposure to IR (1 Gy), U2OS and U2OS-hTR cells treated with siLuc recruit 53BP1 to DNA damage sites within 15 min of exposure, whereas siNHP2-treated U2OS and U2OS-hTR cells show a delayed recruitment of 53BP1, peaking between 1 to 2 h post-IR (Fig 8F and G, p<0.0001). Importantly, the observed impact of NHP2 depletion on 53BP1 recruitment in U2OS cells – that do not express h*TR* – provides another strong argument in favor of an h*TR*-independent role for NHP2 in regulating DDR. Interestingly, γ-H2AX foci formation was also defective in NHP2-depleted cells recovering from IR, suggesting a general impact of NHP2 on DDR pathways (Supplementary Fig S9A and B).

Collectively, our results suggest that the downregulation of NHP2 expression in hTR$^+$/ALT$^+$ cells reduces DDR activation at telomeres.

Discussion

Replicative immortality was discovered several decades ago as a commonplace mechanism in most cancer cells to circumvent the chromosome end replication problem and thus, proliferate indefinitely (Hanahan & Weinberg, 2011). Two distinct pathways have been discovered so far that ensure telomere maintenance in indefinitely dividing cancer cells: either telomerase reactivation or activation of an ALTernative mechanism of telomere maintenance. An accumulating body of evidence suggests that these two pathways are mutually exclusive

and cannot co-exist in the same cell, at least under the physiological conditions of telomerase expression (Claude & Decottignies, 2020).

Telomerase is reactivated by de-repressing the h*TERT* gene that, while highly expressed in germline and embryonic stem cells, gets silenced epigenetically in normal somatic cells (Yuan *et al*, 2019; Jafri *et al*, 2016; Pestana *et al*, 2017). Conversely, expression of the h*TR* gene, that encodes the RNA subunit of the telomerase holoenzyme, is permanently maintained in differentiated cells (Takakura *et al*, 1998; Cong *et al*, 2002). Loss of telomerase activity in normal somatic cells has long been considered as a protective mechanism against the uncontrolled proliferation, seen otherwise in transformed cells. Why normal cells silence h*TERT*, and not h*TR*, can be at least partly explained by the observation that h*TR* protects cells from apoptosis, through undefined – but telomerase-independent – mechanisms (Gazzaniga & Blackburn, 2014; Kedde *et al*, 2006).

The second pathway leading to replicative immortality of cancer cells is the ALT pathway. Activation of ALT requires several genetic, epigenetic and post-translational alterations that, together, convert the DNA repair-resistant ends of chromosomes into recombination-prone structures (Cesare & Reddel, 2010; Dilley & Greenberg, 2015; Henson *et al*, 2002). Since the h*TR* gene was cloned before h*TERT*, the initial discovery of human ALT^+ cells was based on the lack of expression of the h*TR* subunit in some immortalized human cell lines (Bryan *et al*, 1997). Later, as ALT^+ cells turned out to also lack h*TERT* mRNA, the silencing of h*TR* could not be explained solely by a need to repress telomerase activity but rather suggested additional ALT-promoting functions. h*TR* silencing however is not a general hallmark of ALT^+ cell lines: previous reports of hTR^+/ALT^+ cell lines (Perrem *et al*, 2001; Tilman *et al*, 2009), together with our two in-house derived ALT^+ sarcoma cell lines, demonstrate that ALT^+ cell viability is in fact, compatible with h*TR* expression. In those cells however, we detected significantly reduced levels of NHP2 protein.

Here, we took advantage of the twenty-year old, elegant system of cellular hybrids between TEL^+ and ALT^+ cells (Perrem *et al*, 1999) to study how these hybrid cells, conflicted with the initial h*TERT* and h*TR* gene expressions in an ALT background, eventually find their way to proficient proliferation using the ALT mechanism. Through two independent cellular hybridization procedures, we obtained two ALT^+ hybrids that, while retaining h*TERT* expression, had both repressed telomerase activity, but through distinct mechanisms. In the first ALT^+ hybrid, we observed a progressive silencing of the h*TR* gene promoter while, in the second one, significant levels of h*TR* RNA were maintained. Although the protein levels of NHP2, an h*TR*

chaperone necessary for the proper assembly and activity of the telomerase complex (Wang & Meier, 2004; Fu & Collins, 2006, 2007), were found to be downregulated in that second hybrid, ectopic NHP2 overexpression did not rescue telomerase activity. The mechanisms of telomerase activity repression in that hybrid thus remain to be elucidated. This finding however seemingly recapitulated the cellular events occurring in some h*TR*-expressing ALT$^+$ cancer cells wherein we observed a similar reduction in NHP2 protein levels. h*TR*-expressing cancer cells differ however from the hybrid cells in one important aspect: they do not reduce NHP2 levels to just suppress telomerase activity, as they likely never reactivated h*TERT* expression during the oncogenic process.

Why then do h*TR*-expressing ALT$^+$ cells suppress NHP2 protein expression if h*TERT* is not expressed? Clues to answer this question came after we first observed that the ectopic expression of h*TR* in ALT$^+$/hTR$^-$ cells upregulates 53BP1 recruitment at telomeres. This was associated with a downregulation of telomeric p-RPA^{S33} and a concomitant reduction in RAD51 recruitment. This, in turn, likely reduced the cell's ability to effectively regress and repair the stalled replication forks at telomeres, while increasing the occurrence of fork collapses marked by 53BP1. In this context, cells may become heavily dependent on break-induced replication to repair the collapsed forks, generating more C-circles in a POLD3-dependent manner (Fig 9). Alternatively, the reduced ATR signaling at telomeres of h*TR*-expressing ALT$^+$ cells, accompanied with a reduced recruitment of RAD51 as we showed, may result in an increased abundance of telomeric C-overhang formation and thus, increased C-circle generation as reported before (Oganesian & Karlseder, 2011).

Previously, h*TR* was proposed to act as a negative regulator of ATR kinase (Kedde *et al*, 2006), but we did not observe a global repression of ATR kinase activity upon ectopic expression of h*TR* in ALT$^+$/hTR$^-$ cells. Our data indicate that the impact of h*TR* on ATR signaling, through a modulation of p-RPA^{S33} levels, is telomere-specific and results from the h*TR*-activated and DNA-PK/hnRNPA1-dependent depletion of RPA from telomeres. We propose that, through its previously reported interaction with the KU subunits of the DNA-PK complex (Ting *et al*, 2005) and the reported role of DNA-PK/hnRNPA1 in removing RPA from telomeres (Ting *et al*, 2009; Flynn *et al*, 2011; Le *et al*, 2013), h*TR* therefore indirectly reduces ATR activation at ALT telomeres. Our observation that, in U2OS/ALT$^+$/hTR$^-$ cells, hnRNPA1 knock-down or DNA-PKcs inhibition shows the opposite impact on telomeric RPA abundance suggests that, in the absence of h*TR*, the DNA-PK/hnRNPA1 complex is not able to facilitate the RPA-to-POT1 switch. Importantly, both Flynn *et al* (2011) and Sui *et al* (2015) investigated

this switch in TEL^+ cells that express h*TR*. In future, it would be interesting to investigate this further and to understand why DNA-PK/hnRNPA1 inactivation reduces telomeric RPA abundance in U2OS/ALT^+/hTR^- cells. Overall, it is intriguing to observe that h*TR* silencing offers to ALT^+ cells the possibility to deregulate the function of the DNA-PK/hnRNPA1 complex at telomeres, resulting in an increased abundance of telomeric RPA foci, and thus promoting further the recruitment of HR machinery for telomeric recombination.

Since the recruitment of 53BP1 to defective telomeres is typically a signal for senescence or apoptosis and is incompatible with a smooth proliferation of cells (Artandi & Depinho, 2010; Kaul *et al*, 2012; Fernandez-Vidal *et al*, 2017), h*TR*-expressing ALT^+ cells are forced to set up mechanisms to reduce TIF. We found that one such natural adaptation to reduce TIF is through the downregulation of NHP2 protein levels. NHP2 depletion, with siRNAs, indeed significantly reduces the recruitment of 53BP1 DNA damage marker to the telomeres of ALT^+ cells. NHP2 – and some other h*TR* chaperones – were previously reported to play a role in propagating effective DDR following chemically-induced DNA damage (Lin *et al*, 2015). We have found that h*TR*-expressing ALT^+ cells, with persistent telomeric DNA damages, also depend on NHP2 for successful propagation of 53BP1 signals. More generally, our data indicate that NHP2 plays a key role in the timely recruitment of both 53BP1 and γ-H2AX foci to sites of DNA DSBs post-IR treatment. This unexpected role for NHP2 in DDR pathway activation, which we found to be independent from h*TR*'s impact on telomeric p-RPA^{S33} abundance, could nevertheless be related to its role as RNA-binding protein. Along this line, NHP2 was recently shown to interact with other RNA molecules like ribosomal RNA (Benyelles *et al*, 2020). Several RNA binding proteins have been recently identified as novel players in the RNA-dependent DNA repair pathway. In fact, 53BP1 recruitment to sites of DNA DSBs has been shown to be dependent on damage-induced long non-coding RNAs and small non-coding RNAs (Michelini *et al*, 2017; Francia *et al*, 2012, 2016). Exactly where NHP2 fits into this pathway is a question that warrants further detailed investigation.

The silencing of h*TR* gene in a subset of ALT^+ cell lines is in apparent contradiction with the observation that h*TR* is required to protect cells against apoptosis (Gazzaniga & Blackburn, 2014). Using siRNAs that efficiently deplete h*TR* from cells, we found however that, even if expressed at barely detectable levels, the RNA is sufficient to protect "hTR^-/ALT^+" cells from cell death. Our data did not support the hypothesis that the death of h*TR*-depleted cells results from ATR hyper-activation and further experiments are needed to understand the underlying mechanisms.

Altogether, our study further deciphers the interplay between telomerase and ALT pathways by providing new evidences of the incompatibility between telomerase subunits and the recombination-mediated mechanism of telomere elongation, through non-canonical functions of h*TR* (Fig 9). Furthermore, we have uncovered a new role for NHP2 as an activator of 53BP1 signaling at dysfunctional ALT telomeres, thus providing a mechanistic explanation to its observed natural downregulation in h*TR*-expressing ALT^+ cells. This work strengthens the links between non-coding RNAs and the DNA damage response at telomeres and suggests that DDR hyper-activation, through the modulation of RNA signaling, may represent a valid option for future therapies targeting ALT^+ cells with inherent replication problems at telomeres.

Materials and Methods

For reagents that are not commonly used, details are provided in Table 1.

Table 1. Specific reagents used in this study.

Chemicals, Enzymes and other reagents	Source	Catalog number
MG132 proteasome inhibitor	Sigma-Aldrich	474790
Complete Mini protease inhibitors	Sigma-Aldrich	11836153001
Hygromycin B	Sigma-Aldrich	H3274
Puromycin	MP Biomedicals	210055225
Lipofectamine 2000	Thermo Fisher Scientific	11668019
Polyethylenimine, linear, MW 25000 (PEI 25K)	Polysciences, Inc.	23966-1
TriPure Isolation Reagent	Sigma-Aldrich	11667165001
Poly-L-Lysine HydroBromide	Sigma-Aldrich	P2636
AEBSF serine protease inhibitor	Sigma-Aldrich	SBR00015
M-MLV reverse transcriptase	Thermo Fisher Scientific	28025-013
Exonuclease III	New England Biolabs	M0206S
Phi29 polymerase	New England Biolabs	M0269L
Blocking Reagent	Sigma-Aldrich	11096176001
BrdU	MP Biomedicals	100166
BrdC	Sigma-Aldrich	B5002
Colcemid	Sigma-Aldrich	10295892001
Hoechst 33258	Sigma-Aldrich	94403
RO-3306 CDK1 inhibitor	Selleckchem	S7747
Normal goat serum	Cell Signaling Technology	5425S
VE-821 ATR kinase inhibitor	Selleckchem	S8007
KU5593 ATM kinase inhibitor	Selleckchem	S1092
Nu7026 DNA-PK inhibitor	Selleckchem	S2893
One Day ChIP kit	Diagenode	C01010080
Doxorubicin hydrochloride	Sigma-Aldrich	D1515
Click-iT EdU Cell Proliferation Kit	Thermo Fisher Scientific	C10337
Genopure Plasmid Midi Kit	Sigma-Aldrich	03 143 414 001
KAPA SYBR FAST	Sigma-Aldrich	KK4602
SuperSignal West Pico Chemiluminescent Substrate	Thermo Fisher Scientific	34580
Telo*TAGGG* Telomere Length Assay	Sigma-Aldrich	12209136001
QX200™ ddPCR™ EvaGreen Supermix	Bio-Rad	1864034
QX200™ Droplet Generation Oil for EvaGreen	Bio-Rad	1864005

Cell Culture

SW39/TEL$^+$ (kindly provided by W. Wright, UT Southwestern, Dallas, USA) and IMRB/ALT$^+$ (Coriell Institute for medical Research, New Jersey, USA) cell lines derived from IMR90 human fetal lung fibroblasts have been described previously (Tilman *et al*, 2009). Two independent cellular hybridizations were performed between SW39/TEL$^+$ and IMRB/ALT$^+$ cells through the

procedure described in Episkopou *et al* (2014 and 2019). SI14/TEL$^+$ and SI24/ALT$^+$ hybrids were obtained from the 1st hybridization; 6C3/TEL$^+$ and 8G12/ALT$^+$ were generated during the 2nd hybridization. VA13/ALT$^+$ are SV40T-immortalized human fetal lung fibroblasts (Tilman *et al*, 2009). All the above cell lines were cultured in EMEM supplemented with 10% FBS (Gibco), 1% NEAA (Gibco) and 1% penicillin/streptomycin (Gibco) and grown at 37°C with 5% CO_2. HEK293-T (ATCC, CRL-3216) and the osteosarcoma cell lines, U2OS/ALT$^+$ (ATCC, HTB-96), SaOS-2/ALT$^+$ (ATCC, CRL-7939) and 143B/TEL$^+$ (Coriell Institute for medical Research, New Jersey, USA) were grown at 37°C in DMEM (Gibco) supplemented with 10% FBS (Gibco), 1% glutamine (Gibco) and 1% penicillin/streptomycin (Gibco). LB23/TEL$^+$ and LB188/ALT$^+$ rhabdomyosarcoma cell lines, described previously (Tilman *et al*, 2009), were grown at 37°C in IMDM medium (Gibco) supplemented with 10% FBS (Gibco), 1% NEAA (Gibco) and 1% penicillin/streptomycin (Gibco). The LB857/ALT$^+$ cell line, established from a myxoid sarcoma and kindly provided by M. Swinarska and F. Brasseur (Ludwig Institute for Cancer Research, Brussels), was grown in the same conditions.

Transfections

siRNAs were transfected at a final concentration of 100 nM, using reverse transfection protocol with Lipofectamine 2000 (Thermo Fisher Scientific) as per manufacturer's instructions. For all experiments, cells were collected 3 days post-transfection, unless indicated otherwise. All siRNAs are listed in Table 2. For plasmid transfections, 2 µg of plasmid and 6 µl of 1 mg/ml PEI stock solution were mixed in 200 µl of serum-free OPTI-MEM medium (Invitrogen), incubated at RT for 20 min and added to cells (plated in 6-well plates the day before) in 1.8 ml medium supplemented with 10% FBS. Six hours later, the PEI-containing medium was removed and replaced with fresh medium. Plasmids used were: pBabe::*U1-hTR-hygro* (Tilman *et al*, 2009) and pLenti7.3-EmGFP::NHP2 (kindly provided by Patrick Revy, Institut Imagine, Paris, France).

Table 2. siRNAs used in this study.

siRNA	Reference
siLuc: CUUACGCUGAGUACUUCGA	Arnoult *et al*, 2012
sihTR#1: GUCUAACCCUAACUGAGAA	Kedde *et al*, 2006
sihTR#2: GCAAACAAAAAAUGUCAGCU	Kedde *et al*, 2006
siNHP2: UCUUGAUGCAUUUGUAGAGCU	Benyelles *et al*, 2020
siATR: CCUCCGUGAUGUUGCUUGA	Flynn *et al*, 2015
siPOLD3: GGCCUCUGUUCAAUACUGA	Zhang *et al*, 2019a
siSMARCAL1: UUGCUAAGAAGGUCAAAGC	Zhang *et al*, 2019b
sihnRNPA1: UCCACGACCACCACCAAAG	Flynn *et al*, 2011

Lentiviral infections and selection

For viral particle generation, HEK293-T cells were transfected with pLenti7.3-EmGFP::NHP2, pCMV-dR8.2 dvpr (Addgene #8455) and pCMV-VSV-G (Addgene #8454) for 48 h. The supernatant from the transfected cells containing the viral particles was filtered and incubated with polybrene (8µg/ml) for 20 min at RT. Infection was carried out by replacing the medium of the target cell line with virus containing-medium for 24 h. FACS analysis validated cells for GFP expression, indicating NHP2 co-expression.

RNA extraction and qRT-PCR

RNA was extracted from cells using TriPure Isolation Reagent (Sigma-Aldrich) according to the manufacturer's instructions. Subsequently, 1 µg of RNA was retro-transcribed with MMLV-RT (Thermo Fisher Scientific) and random hexamers (Thermo Fisher Scientific) for cDNA synthesis, according to the manufacturer's instructions. qPCRs were performed using KAPA SYBR FAST (Sigma-Aldrich). All primers are described in Table 3.

Table 3. Primers used in this study.

Primer	Sequence (5' to 3')	Reference
hTERT-F	CGGAAGAGTGTCTGGAGCAA	Tilman *et al*, 2009
hTERT-R	GGATGAAGCGGAGTCTGG	Tilman *et al*, 2009
hTR-F	TTTGTCTAACCCTAACTAACTGAGAAG	Tilman *et al*, 2009
hTR-R	TTGCTCTAGAATGAACGGTGGA	Tilman *et al*, 2009
hnRNPA1-F	AAGCAATTTTGGAGGTGGTG	Kress *et al*, 2005
hnRNPA1-R	ATAGCCACCTTGGTTTCGTG	Kress *et al*, 2005
NHP2-F	GAGCTGCTGGTCAACCAGAA	This study
NHP2-R	CTTGATGCATTTGTAGAGCT	This study
ACTB-F	TGTACGCCAACACAGTGCTG	Boros *et al*, 2014
ACTB-R	GCTGGAAGGTGGACAGCGA	Tilman *et al*, 2009
PML-F	TGTACCGGCAGATTGTGGAT	Fu *et al,* 2015
PML-R	AGATGTTGTTGGTCTTGCG	Fu *et al,* 2015
hTR ChIP-F	CCCGCCCGAGAGAGTGAC	Atkinson *et al*, 2005
hTR ChIP-R	AAGTCAGCGAGAAAAACAGC	Atkinson *et al*, 2005
4qHox ChIP-F	CCGCGTCCGTCCGTGAAA	Boros *et al*, 2014
4qHox ChIP-R	TCCGTCGCCGTCCTCGTC	Boros *et al*, 2014
c-fos ChIP-F	GAGCAGTTCCCGTCAATCC	Yang & Sharrocks, 2005
c-fos ChIP-R	GCATTTCGCAGTTCCTGTCT	Yang & Sharrocks, 2005
hnRNPA1-ChIP-F	CATGCTTTGCCAAGCGACTTGAC	Fleming *et al*, 2013
hnRNPA1-ChIP-R	GGAGCAAGCTGACGAACGTATC	Fleming *et al*, 2013
TS	AATCCGTCGAGCAGAGTT	Kim & Wu, 1997
ACX	GCGCGG$(CTTACC)_3$CTAACC	Kim & Wu, 1997

Droplet digital telomerase repeat amplification protocol (ddTRAP)

For ddTRAP, we used the protocol previously described by Ludlow *et al* (2018). Briefly, 500 000 cells were lysed in 40 µl NP-40 buffer (10 mM Tris-HCl pH 8.0, 0.1 mM $MgCl_2$, 1 mM EDTA, 10% (v/v) glycerol, 1% (v/v) NP-40, 150 mM NaCl, 0.25 mM sodium deoxycholate, 5 mM β-mercaptoethanol, 0.1 mM AEBSF), on ice for 30 min. 1 µl of the lysate at 2 µg/µl was added to 50 µl of 1x TRAP buffer (200 mM Tris-HCl, pH 8.3, 15 mM $MgCl_2$, 2.5 mM each dNTPs, 200 mM TS primer (Table 3) and 0.4 mg/ml BSA) and extension reaction was performed by incubating the mix at 25 °C for 40 min, followed by deactivation at 95 °C for 5 min. For the droplet digital PCR (ddPCR) reaction, 3 µl lysis-extension mix was added to 1x EvaGreen Supermix (Bio-Rad), 50 nM TS primer, 50 nM ACX primer (Table 3) in a 20 µl reaction. PCR reaction was performed as follows: initial denaturation for 5 min at 95°C followed by 40 cycles of 95°C/30 sec, 54°C/30 sec and 72°C/30 sec.

Chromatin Immunoprecipitation (ChIP)

Chromatin immunoprecipitation was carried out using OneDay ChIP kit (Diagenode) as per manufacturer's instruction and as described previously (Boros *et al*, 2014). Antibodies are described in Table 4. Immunoprecipitated DNA was analyzed by qPCR with primers described in Table 3.

Genomic DNA extraction

Genomic DNA was extracted from various cell lines by overnight digestion at 45°C with 100 µg/ml of proteinase K and 50 µM $CaCl_2$ in 600 µl lysis buffer (10 mM Tris-HCl, 10 mM EDTA, 5% SDS, pH 8.0) followed by DNA purification with phenol-chloroform-isoamyl alcohol (25:24:1, Sigma-Aldrich) and isopropanol precipitation in 0.3 M sodium acetate (pH 5.2). gDNA was subsequently treated with 0.1 mg/ml RNAse A for 1 hour at 37°C, purified and precipitated again as described above.

Telomere restriction fragment (TRF) analysis

Southern blot using a radioactive $(CCCTAA)_4$ probe was used for TRF analysis, as described previously (Viceconte *et al*, 2017). For TRF, 10 µg RNAse-treated gDNA were digested

overnight with 20 U *Hinf*I and 20 U *Rsa*I, and loaded directly on a 0.8% agarose gel in TAE 1x buffer. Gel migration was performed for 6 hours at 75 V. DIG markers from the Telo*TAGGG* kit were included. Subsequent processing – gel treatment, capillary transfer and pre-hybridization – were performed according to the Telo*TAGGG* kit's instructions. The membrane was hybridized with the radioactive telomere probe for 16 h at 42°C in ULTRAhyb-Oligo hybridization buffer (Ambion). The telomeric probe $(CCCTAA)_4$ was prepared as follows: 10 μM probe was denatured for 5 min at 68°C and 1 μl of the probe was radioactively labeled with 6 μl of [γ-^{32}P] ATP (10 mCi/ml) (Perkin-Elmer) catalyzed by 1 μl T4 poly-nucleotide kinase (Sigma-Aldrich) (10 U/μl) in a 20 μl-reaction mix containing 1x PNK buffer; this mix was incubated for 20 min at 37°C and T4 PNK was then inactivated by the addition of 2 μl of EDTA (0.5 M, pH 8.0). 40 μl of 1x PNK buffer were then added to the radioactive probe before purification on a G-25 column. Post-hybridization, the membrane was washed first with Stringent wash buffer I for 20 min at RT and then with pre-warmed Stringent wash buffer II for 10 min at 42°C (buffers provided in the Telo*TAGGG* kit) and revealed using a Phosphorimager.

C-circle formation assay

C-circle assay was performed as described in Henson *et al* (2017). Briefly, 5 μg of RNA-free genomic DNA were digested with *Hinf*I/*Rsa*I and purified using phenol-chloroform extraction. 10 μl (30 ng) of *Hinf*I/*Rsa*I-digested, purified gDNA were added to 10 μl reaction mix (4 μg/ml BSA, 0.1% Tween-20, 1 mM each dATP, dGTP and dTTP, 1x Phi29 Buffer and 7.5 U Phi29 DNA polymerase); samples were incubated at 30°C for 8 h, then at 65°C for 20 min. The amplification products were slot-blotted on a Hybond N+ nylon membrane (GE Healthcare) and hybridized with the radioactive $(CCCTAA)_4$ probe as described above.

Slot Blot assay for genomic DNA

Genomic DNA samples were prepared ad described for TRF analysis. Varying quantities of digested genomic DNA (50 ng, 100ng, 250ng, 500ng) were denatured with 0.1M NaOH (100°C for 10 min), cooled directly on ice and neutralized with 6X SSC with 0.2 M Tris (pH 7.4). The samples were then slot-blotted onto a Hybond N^+ nylon membrane and hybridized with radioactive $(CCCTAA)_4$ as described above.

Immunofluorescence (IF), native FISH and denaturing DNA-FISH

IF was performed as described previously (Episkopou *et al*, 2019) using antibodies listed in Table 4. Telomeric sequences were detected via hybridization with a TeloG Exiqon LNA^{TM}red probe: (TAMRA) GGGTtAGGGttAGgGTTAGGGttAGGGttAGGGtTA (TAMRA) (small letters indicate LNA^{TM} modified bases). Briefly, cells seeded on 4-well slides the day before were washed twice with PBS and cytoplasm was pre-extracted with permeabilization buffer (20 mM Tris-HCl pH 8.0, 50 mM NaCl, 3 mM $MgCl_2$, 300 mM sucrose, 0.5% Triton X-100). Once fixed with 3.7% formaldehyde and 2% sucrose in PBS 1x for 15 min at RT, cells were washed with 1x PBS and permeabilized again for 10 min at RT. Following 3 washes with 1x PBS, cells were blocked for 1 h at 37°C with blocking solution (10% normal goat serum, 1% BSA, 0.1% Triton X-100 in PBS) and subsequently treated with primary antibodies in the Blocking solution overnight at 4°C. All antibodies used along with the corresponding dilutions can be found in Table 4. The next day, cells were washed 3 times with PBS-Tween (0.1%) at 45°C and incubated with the secondary antibody for 40 min at 37°C. Cells were washed again 3 times with PBS-Tween (0.1%) at 45°C followed by 3 washes with 1x PBS at RT. For POLD3-RAP1 co-staining, both antibodies were added together, overnight in 5% BSA-PBS-Tween (0.1%) solution as described previously (Silva *et al*, 2019). The next day, cells were washed 3 times with PBS-Tween (0.1%) at RT for 10 min each and incubated with the secondary antibody for 1 h at RT. Subsequently, cells were washed again 3 times with PBS-Tween (0.1%) and 3 times with 1x PBS at RT, 10 min and 5 min each, respectively. In the absence of FISH, cells were air dried and mounted with 20-25 µl/well mounting medium (23.5 mg/ml DABCO (Sigma-Aldrich), 20 mM Tris-HCl pH 7.4, 90% v/v glycerol) containing 0.6 µg/ml DAPI.

For telomeric-DNA FISH after IF, cells were re-fixed for 2 min with 3.7% formaldehyde in 1x PBS and incubated with 0.1 mg/ml RNAse A for 1 h at RT. Cells were then washed 3 times with 2x SSC, re-permabilized for 10 min, briefly washed with 1x PBS and fixed again with 3.7% formaldehyde. Cells were serially dehydrated, 2 min each, with 70%, 80%, 90% and 100% ethanol, air dried, overlaid with 35 µl hybridization solution (160 nM TeloG Exiqon LNA^{TM}red probe, 50% deionized formamide, SSC 2x, Blocking reagent 1x) and incubated at 83°C for 3 min with a coverslip. For native FISH, cells were incubated for 1 h with the probe under non-denaturing conditions, at room temperature. Then, unbound probe was washed off successively as follows: 2x15 min in 50% formamide, SSC 2x, 20 mM Tris-HCl pH 7.4 and 3x5 min in 150 mM NaCl, 0.05% Tween-20, 50 mM Tris-HCl pH 7.4. Slides were serially dehydrated again and mounted with mounting medium containing DAPI as described above. Images were acquired

with the Cell Observer Spinning Disk confocal microscope (Zeiss) with 100X objective and analyzed using ImageJ software (National Institute of Health), while maintaining the same threshold for samples from the same experiment. Most experiments were repeated at least 3 times (in some cases 2 times) and representative pictures are shown in the figures.

Table 4. Antibodies used in this study.

Antibodies	Source	Catalog Number
Mouse monoclonal anti-β-Actin (WB-1:200,000)	Sigma-Aldrich	A5441
Rabbit polyclonal anti-NHP2 (WB-1:2500)	Proteintech	15128-1-AP
Rabbit polyclonal anti-DKC1 (WB-1:1000)	Santa Cruz	sc-48794
Rabbit polyclonal anti-GAR1 (WB-1:1000)	Abcam	ab188617
Rabbit polyclonal anti-NOP10 (WB-1:1000)	Abcam	ab235339
Rabbit polyclonal anti-HistoneH3 (ChIP-1:100)	Abcam	ab1791
Rabbit polyclonal anti-H3K9me3 (ChIP-1:100)	Millipore	07-442
Rabbit polyclonal anti-NFYB (ChIP-1:100)	Genespin	PAb001
Mouse monoclonal anti-RNA Pol II (ChIP-1:100)	Millipore	05-623
Rabbit polyclonal anti-H3K27me3 (ChIP-1:100)	Diagenode	C15410195
Rabbit polyclonal anti-H3Ac (ChIP-1:100)	Millipore	06-599
Rabbit polyclonal anti-H3K4me3 (ChIP-1:100)	Abcam	ab8580
Rabbit polyclonal anti-RAP1 (IF-1:350)	Bethyl laboratories	A300-306A
Mouse monoclonal anti-POLD3 (IF-1:100)	Novus Biologicals	H00010714-M01
Rabbit monoclonal anti-RAD51 (IF-1:600)	Abcam	EPR4030(3)
Rabbit polyclonal anti-pRPA32-S33 (IF-1:1000, WB-1:6000)	Bethyl Laboratories	A300-246A
Mouse monoclonal anti-RPA32 (9H8) (IF-1:300, WB-1:6000)	Abcam	ab2175
Mouse monoclonal anti-PML (IF-1:100)	Santa Cruz	sc-966
Rabbit polyclonal anti-53BP1 (IF-1:600, WB-1:500)	Novus Biologicals	NB100-304
Goat- anti-rabbit IgG- HRP (WB-1:10,000)	Enzo Life Sciences	ADI-SAB-300-J
Goat anti-mouse IgG- HRP (WB-1: 2000)	Abcam	sc-2005
Goat anti-rabbit IgG- Alexa 488 (IF-1:400)	Thermo Fisher Scientific	A-11008
Goat anti-mouse IgG- Alexa 488- (IF-1:400)	Thermo Fisher Scientific	A-11001
Donkey anti-mouse IgG- Alexa 647 (IF-1:400)	Thermo Fisher Scientific	A-31571
Goat anti-rabbit IgG- Alexa 647 (IF-1:400)	Abcam	ab150087
Rabbit monoclonal anti-pCHK1-S345 (WB-1:6000)	Cell Signalling	2348S
Mouse monoclonal anti-CHK1 (WB 1:2000)	Cell Signalling	2360S
Rabbit monoclonal anti-pATR-T1989 (WB-1:6000)	Genetex	GTX128145
Rabbit polyclonal anti-ATR (WB-1:1000)	Cell Signalling	2790S
Mouse monoclonal anti-Vinculin (WB-1:10000)	Millipore	05386
Mouse monoclonal anti-γH2AX (S-139) (IF-1:1000, WB-1:1000)	Millipore	05-636
Rabbit polyclonal anti-H2AX (WB-1:5000)	Millipore	07-627

Western blotting

Whole cell extracts were prepared by lysing cell pellets in RIPA buffer (150 mM NaCl, 50 mM Tris-HCl pH 8.0, 1% NP-40, 0.5% sodium deoxycholate, 0.1% SDS, 1 mM EDTA). Western blotting was performed according to standard procedures using antibodies listed in Table 4. Blots were revealed with SuperSignal West Pico Chemiluminescent Substrate. Signal quantification was done using ImageJ software. All experiments were repeated at least 3 times and representative blots are shown in the figures.

ALT telomere DNA synthesis in APBs (ATSA)

ATSA was performed as described previously (Zhang *et al*, 2019a). Briefly, cells were plated on poly-L-lysine coated coverslips and synchronized with 2 mM Thymidine for 21 h before release into fresh medium for 4 h. Subsequently, 15 μM CDK1 inhibitor RO-3306 (Selleckchem) was added to the cells for 18 h to synchronize cells in G2/M. At this stage, CDKi-containing medium was removed and replaced by 10 μM EdU-containing medium for 1 h. Cells were fixed and permeabilized as described above before EdU detection using the Click-iT EdU Alexa Fluor 488

Imaging Kit as per manufacturer's instruction. Subsequently, IF-telo FISH was performed as described above. Image acquisition and analysis were as for DNA FISH.

CO-FISH

Cells were incubated with 10 μM BrdU:BrdC (3:1) for 16 h and arrested in metaphase by incubating with 0.2 μg/ml Colcemid (Gibco). Cells were collected after trypsinization and subjected to a hypotonic shock with 0.075 M KCl treatment at 37°C for 30 min before fixation with methanol/acetic acid solution (3:1, v/v) and 3 washes in the same fixation solution. Metaphase spreads were obtained by dropping the fixed cell suspensions onto clean Superfrost slides and dried overnight, protected from light. The slides were treated with 0.1 mg/ml RNase A in PBS for 10 min at 37°C, stained with Hoechst 33258 (0.5 μg/ml in 2x SSC) for 10 min at RT and exposed to 365-nm UV light (Stratalinker 1800 UV irradiator; crosslink at energy=$5.4x10^3$ J/m2). The BrdU/dC substituted DNA strand was digested with Exonuclease III (3 U/μl) for 10 min at 37°C followed by 10 min at RT. The slides were subsequently dehydrated serially with 70%, 90% and 100% ethanol and hybridized with a FITC-OO-$(CCCTAA)_3$ PNA probe (Panagene) in hybridization solution-I (70% deionized formamide, 20 mM Tris pH 7.4, 1x Blocking agent, 25 μM probe) for 1.5 h. The slides were washed for 5 min with 70% formamide,

10 mM Tris-HCl pH 7.4 followed by another wash with 150 mM NaCl, 0.05% Tween-20, 50 mM Tris-HCl pH 7.4 for 5 min. The slides were dehydrated again using the ethanol series (70%, 90% and 100%). Subsequently, the slides were incubated with TeloG Exiqon LNA^{TM}red probe in hybridization solution-II (as described for IF-FISH above) for 1.5 h and rest of the steps were performed as described for the IF-FISH protocol.

Irradiation and 53BP1 or γH2AX IF

U2OS and U2OS-hTR cells, transfected with either siLuc or siNHP2, were plated on poly-L-Lysine-coated cover slips in a 24-well plate and left overnight at 37°C. The next day, the plates with coverslip-containing cells were irradiated (Irradiator: IBL-637) at 1 Gy, and immediately returned to 37°C. At time intervals of 1 min, 30 min, 1-, 2-, 6- and 12- hours, one set of coverslips were fixed and permeabilized as described earlier. Subsequently, the nuclei were stained for 53BP1 or γH2AX and counterstained with DAPI, as described above.

Quantification and Statistical Analysis

ImageJ was used for quantification of western blots and analysis of confocal microscopy pictures. Web tools, Microsoft Excel and Graphpad Prism 8 were used for statistical analyses. Whenever needed, the Shapiro-Wilk test to check for normal distribution of the data and the Bartlett test for comparison of variances between the compared groups were applied. These analyses are provided in the Source data file available online. Statistical analyses include Student's t-test, X^2 test, one- or two-way ANOVA followed by appropriate post-hoc analyses for multiple comparisons, wherever applicable, and are clearly specified in the figure legends. All *p* values ≤0.05 were considered as statistically significant. Whenever possible, exact *p* values are provided in the Source data file available online. Graphs usually indicate mean ± SD (standard deviation) and the number of replicates is provided in the figure legend.

Acknowledgements

We are most grateful to P. Revy (Institut Imagine, Paris, France) for the generous gift of pLenti7.3-EmGFP::NHP2 plasmid and for precious comments on the manuscript. We thank M.

Swinarska, F. Brasseur and W. Wright for cell lines. We are grateful to P. Moureau and J. Ruelle (Cliniques universitaires St-Luc, Brussels) for help with the ddPCR and to A. Diacofotakis for help with statistical analyses. We thank M. Mahieu for help with IF analyses. We thank E. Claude, G. Le Berre and N. Arnoult for careful reading of the manuscript. This study was supported by grants from the Fonds National de la Recherche Scientifique (FNRS), the Télévie/FNRS (M.R., FNRS 7.4506.17; D.G., FNRS 7.4513.19), La Fondation contre le Cancer (2018-072), the de Duve Institute and the D.G. Higher Education and Scientific Research of the French Community of Belgium (Actions de Recherche Concertées) (E.M., ARC 14/19-059). AD is a recipient from the FNRS.

Author contributions

A.D. initiated, supervised and coordinated the project. M.R. and A.D. designed the study, analyzed the data and wrote the paper. M.R, D.G. and E.M. performed the experiments and prepared figures.

Conflict of interest

The authors declare that they have no conflict of interest

References

Arnoult N, Van Beneden A & Decottignies A (2012) Telomere length regulates TERRA levels through increased trimethylation of telomeric H3K9 and HP1α. *Nat Struct Mol Biol* 19: 948-56

Artandi SE & Depinho RA (2010) Telomeres and telomerase in cancer. *Carcinogenesis* 31: 9–18

Atkinson SP, Hoare SF, Glasspool RM & Keith WN (2005) Lack of telomerase gene expression in alternative lengthening of telomere cells is associated with chromatin remodeling of the hTR and hTERT gene promoters. *Cancer Res* 65**:** 7585–7590

Benyelles M, O'donohue M-F, Kermasson L, Lainey E, Borie R, Lagresle-Peyrou C, Nunes H, Cazelles C, Crestani B, De Villartay J-P, Gleizes P-E, Callebaut I, Kannengiesser C & Revy P (2020) NHP2 deficiency impairs rRNA biogenesis and causes pulmonary fibrosis and Høyeraal-Hreidarsson syndrome. *Hum Mol Genet* 29: 907–922

Blackburn EH (1991) Structure and function of telomeres. *Nature* 350: 569–573

Boros J, Arnoult N, Stroobant V, Collet J-F & Decottignies A (2014) Polycomb repressive complex 2 and H3K27me3 cooperate with H3K9 methylation to maintain heterochromatin protein 1 at chromatin. *Mol Cell Biol* 34: 3662–3674

Bower K, Napier CE, Cole SL, Dagg RA, Lau LMS, Duncan EL, Moy EL & Reddel RR (2012) Loss of wild-type ATRX expression in somatic cell hybrids segregates with activation of Alternative Lengthening of Telomeres. *PLoS One* 7: e50062

Bryan TM, Marusic L, Bacchetti S, Namba M & Reddel RR (1997) The telomere lengthening mechanism in telomerase-negative immortal human cells does not involve the telomerase RNA subunit. *Hum Mol Genet* 6: 921–926

Buisson R, Joshi N, Rodrigue A, Ho CK, Kreuzer J, Foo TK, Hardy EJL, Dellaire G, Haas W, Xia B, Masson J-Y & Zou L (2017) Coupling of homologous recombination and the checkpoint ATR. *Mol Cell* 65: 336-346

Cesare AJ, Kaul Z, Cohen SB, Napier CE, Pickett HA, Neumann AA & Reddel RR (2009) Spontaneous occurrence of telomeric DNA damage response in the absence of chromosome fusions. *Nat Struct Mol Biol* 16: 1244–1251

Cesare AJ & Reddel RR (2010) Alternative lengthening of telomeres: Models, mechanisms and implications. *Nat Rev Genet* 11: 319–330

Cho NW, Dilley RL, Lampson MA & Greenberg RA (2014) Interchromosomal homology searches drive directional ALT telomere movement and synapsis. *Cell* 159: 108–121

Claude E & Decottignies A (2020) Telomere maintenance mechanisms in cancer: telomerase, ALT or lack thereof. *Curr Opin Genet Dev* 60: 1–8

Cong Y-S, Wright WE & Shay JW (2002) Human telomerase and its regulation. *Microbiol Mol Biol Rev* 66: 407–425

Couch FB, Bansbach CE, Driscoll R, Luzwick JW, Glick GG, Bétous R, Carroll CM, Jung SY, Qin J, Cimprich KA & Cortez D (2013) ATR phosphorylates SMARCAL1 to prevent replication fork collapse. *Genes Dev* 27: 1610–1623

Cox KE, Maréchal A & Flynn RL (2016) SMARCAL1 resolves replication stress at ALT telomeres. *Cell Rep* 14: 1032–1040

Dilley RL & Greenberg RA (2015) ALTernative telomere maintenance and cancer. *Trends in Cancer* 1: 145–156

Dilley RL, Verma P, Cho NW, Winters HD, Wondisford AR & Greenberg RA (2016) Break-induced telomere synthesis underlies alternative telomere maintenance. *Nature* 539: 54–58

Dunham MA, Neumann AA, Fasching CL & Reddel RR (2000) Telomere maintenance by recombination in human cells. *Nat Genet* 26: 447–450

Episkopou H, Draskovic I, Van Beneden A, Tilman G, Mattiussi M, Gobin M, Arnoult N, Londoño-Vallejo A & Decottignies A (2014) Alternative lengthening of telomeres is characterized by reduced compaction of telomeric chromatin. *Nucleic Acids Res* 42:4391-4405.

Episkopou H, Diman A, Claude E, Viceconte N & Decottignies A (2019) TSPYL5 depletion induces specific death of ALT cells through USP7-dependent proteasomal degradation of POT1. *Mol Cell* 75: 469-482.e6

Fernandez-Vidal A, Vignard J & Mirey G (2017) Around and beyond 53BP1 nuclear bodies. *Int J Mol Sci* 18: 2611

Fleming JD, Pavesi G, Benatti P, Imbriano C, Mantovani R & Struhl K (2013) NF-Y coassociates with FOS at promoters, enhancers, repetitive elements, and inactive chromatin regions, and is stereo-positioned with growth-controlling transcription factors. *Genome Res.* 23**:** 1195–1209

Flynn RL, Centore RC, O'Sullivan RJ, Rai R, Tse A, Songyang Z, Chang S, Karlseder J, Zou L (2011) TERRA and hnRNPA1 orchestrate an RPA-to-POT1 switch on telomeric single-stranded DNA. Nature 471: 532-536

Flynn RL, Cox KE, Jeitany M, Wakimoto H, Bryll AR, Ganem NJ, Bersani F, Pineda JR, Suvà ML, Benes CH, Haber DA, Boussin FD & Zou L (2015) Alternative lengthening of telomeres renders cancer cells hypersensitive to ATR inhibitors. *Science* 347: 273–277

Francia S, Cabrini M, Matti V, Oldani A & d'Adda di Fagagna F (2016) DICER, DROSHA and DNA damage response RNAs are necessary for the secondary recruitment of DNA damage response factors. *J Cell Sci* 129: 1468–1476

Francia S, Michelini F, Saxena A, Tang D, De Hoon M, Anelli V, Mione M, Carninci P & d'Adda di Fagagna F (2012) Site-specific DICER and DROSHA RNA products control the DNA-damage response. *Nature* 488: 231–235

Fu D & Collins K (2006) Human telomerase and Cajal body ribonucleoproteins share a unique specificity of Sm protein association. *Genes Dev* 20: 531–536

Fu D & Collins K (2007) Purification of human telomerase complexes identifies factors involved in telomerase biogenesis and telomere length regulation. *Mol Cell* 28: 773–785

Fu S, Wei J, Wang G, Wang B, Wang Y, Lai X & Huang H (2015) The key role of PML in IFN-α induced cellular senescence of human mesenchymal stromal cells. *Int J Oncol* 46: 351-359

Gazzaniga FS & Blackburn EH (2014) An antiapoptotic role for telomerase RNA in human immune cells independent of telomere integrity or telomerase enzymatic activity. *Blood* 124: 3675–3684

Greider CW & Blackburn EH (1985) Identification of a specific telomere terminal transferase activity in tetrahymena extracts. *Cell* 43: 405–413

Grudic A, Jul-Larsen A, Haring SJ, Wold MS, Lønning PE, Bjerkvig R & Bøe SO (2007) Replication protein A prevents accumulation of single-stranded telomeric DNA in cells that use alternative lengthening of telomeres. *Nucleic Acids Res* 35: 7267–7278

Hanahan D & Weinberg RA (2011) Hallmarks of cancer: the next generation. *Cell* 144: 646–674

Heaphy CM, Subhawong AP, Hong SM, Goggins MG, Montgomery EA, Gabrielson E, Netto GJ, Epstein JI, Lotan TL, Westra WH, Shih IM, Iacobuzio-Donahue CA, Maitra A, Li QK, Eberhart CG, Taube JM, Rakheja D, Kurman RJ, Wu TC, Roden RB, *et al* (2011) Prevalence of the alternative lengthening of telomeres telomere maintenance mechanism in human cancer subtypes. *Am J Pathol* 179: 1608–1615

Henson JD, Cao Y, Huschtscha LI, Chang AC, Au AYM, Pickett HA & Reddel RR (2009) DNA C-circles are specific and quantifiable markers of alternative- lengthening-of-telomeres activity. *Nat Biotechnol* 27: 1181–1185

Henson JD, Lau LM, Koch S, Martin La Rotta N, Dagg RA & Reddel RR (2017) The C-Circle assay for alternative-lengthening-of-telomeres activity. *Methods* 114: 74–84

Henson JD, Neumann AA, Yeager TR & Reddel RR (2002) Alternative lengthening of telomeres in mammalian cells. *Oncogene* 21: 598–610

Hsu K-S & Kao H-Y (2018) PML: regulation and multifaceted function beyond tumor suppression. *Cell Biosci* 8: 5

Jafri MA, Ansari SA, Alqahtani MH & Shay JW (2016) Roles of telomeres and telomerase in cancer, and advances in telomerase-targeted therapies. *Genome Med* 8:69

Kaul Z, Cesare AJ, Huschtscha LI, Neumann AA & Reddel RR (2012) Five dysfunctional telomeres predict onset of senescence in human cells. *EMBO Rep* 13: 52–59

Kedde M, Le Sage C, Duursma A, Zlotorynski E, Van Leeuwen B, Nijkamp W, Beijersbergen R & Agami R (2006) Telomerase-independent regulation of ATR by human telomerase RNA. *J Biol Chem* 281: 40503–40514

Kidiyoor GR, Kumar A & Foiani M (2016) ATR-mediated regulation of nuclear and cellular plasticity. *DNA Repair* 44: 143-150

Kim NW & Wu F (1997) Advances in quantification and characterization of telomerase activity by the telomeric repeat amplification protocol (TRAP). *Nucleic Acids Res* 25: 2595–2597

Kress E, Baydoun HH, Bex F, Gazzolo L, Duc Dodon M (2005) Critical role of hnRNPA1 in HTLV-1 replication in human transformed T lymphocytes. *Retrovirology* 2:8

Le PN, Maranon DG, Altina NH, Battaglia CLR & Bailey SM (2013) TERRA, hnRNPA1, and DNA-PKcs interactions at human telomeres. *Front Oncol* 3: 91

Lin P, Mobasher ME, Hakakian Y, Kakarla V, Naseem AF, Ziai H & Alawi F (2015) Differential requirements for H/ACA ribonucleoprotein components in cell proliferation and response to DNA damage. *Histochem Cell Biol* 144: 543–558

Loe TK, Zhou Li JS, Zhang Y, Azeroglu B, Boddy MN & Denchi EL (2020) Telomere length heterogeneity in ALT cells is maintained by PML-dependent localization of the BTR complex to telomeres. *Genes Dev* 34: 650–662

Lu R, O'Rourke JJ, Sobinoff AP, Allen JAM, Nelson CB, Tomlinson CG, Lee M, Reddel RR, Deans AJ & Pickett HA (2019) The FANCM-BLM-TOP3A-RMI complex suppresses alternative lengthening of telomeres (ALT). *Nat Commun* 10:2252

Ludlow AT, Shelton D, Wright WE & Shay JW (2018) DdTRAP: A method for sensitive and precise quantification of telomerase activity. *Methods Mol Biology* 513–529.

MacNeil DE, Bensoussan HJ & Autexier C (2016) Telomerase regulation from beginning to the end. *Genes* 7: 64

Martínez P & Blasco MA (2015) Replicating through telomeres: a means to an end. *Trends Biochem Sci* 40: 504–515

McNees CJ, Tejera AM, Martínez P, Murga M, Mulero F, Fernandez-Capetillo O & Blasco MA (2010) ATR suppresses telomere fragility and recombination but is dispensable for elongation of short telomeres by telomerase. *J Cell Biol* 188: 639–652

Michelini F, Pitchiaya S, Vitelli V, Sharma S, Gioia U, Pessina F, Cabrini M, Wang Y, Capozzo I, Iannelli F, Matti V, Francia S, Shivashankar G V, Walter NG & d'adda di Fagagna F (2017) Damage-induced lncRNAs control the DNA damage response through interaction with DDRNAs at individual double-strand breaks. *Nat Cell Biol* 19: 1400–1411

Min J, Wright WE & Shay JW (2017) Alternative lengthening of telomeres Mediated by mitotic DNA synthesis engages break-induced replication processes. *Mol Cell Biol* 37: e00226-17

Mokrani-Benhelli H, Gaillard L, Biasutto P, Le Guen T, Touzot F, Vasquez N, Komatsu J, Conseiller E, Pïcard C, Gluckman E, Francannet C, Fischer A, Durandy A, Soulier J, de Villartay J-P, Cavazzana-Calvo M & Revy P (2013) Primary microcephaly, impaired DNA replication, and genomic instability caused by compound heterozygous ATR mutations. *Hum Mutat* 34: 374–384

Mutreja K, Krietsch J, Hess J, Ursich S, Berti M, Roessler FK, Zellweger R, Patra M, Gasser G & Lopes M (2018) ATR-mediated global fork slowing and reversal assist fork traverse

and prevent chromosomal breakage at DNA interstrand cross-links. *Cell Rep* 24: 2629-2642.e5

Nandakumar J & Cech TR (2013) Finding the end: recruitment of telomerase to telomeres. *Nat Rev Mol Cell Biol* 14: 69–82

Neelsen KJ, Zanini IMY, Herrador R & Lopes M (2013) Oncogenes induce genotoxic stress by mitotic processing of unusual replication intermediates. *J Cell Biol* 200: 699–708

O'Sullivan RJ & Karlseder J (2010) Telomeres: protecting chromosomes against genome instability. *Nat Rev Mol Cell Biol* 11: 171–181

Oganesian L & Karlseder J (2011) Mammalian 5′ C-rich telomeric overhangs are a mark of recombination-dependent telomere maintenance. *Mol Cell* 42: 224–236

Olson E, Nievera CJ, Klimovich V, Fanning E & Wu X (2006) RPA2 is a direct downstream target for ATR to regulate the S-phase checkpoint. *J Biol Chem* 281: 39517–39533

Palm W & de Lange T (2008) How shelterin protects mammalian telomeres. *Annu Rev Genet* 42: 301–334

Pan X, Drosopoulos WC, Sethi L, Madireddy A, Schildkraut CL & Zhang D (2017) FANCM, BRCA1, and BLM cooperatively resolve the replication stress at the ALT telomeres. *Proc Natl Acad Sci USA* 114: E5940–E5949

Pennarun G, Hoffschir F, Revaud D, Granotier C, Gauthier LR, Mailliet P, Biard DS, Ois F & Boussin D (2010) ATR contributes to telomere maintenance in human cells. *Nucleic Acids Res* 38: 2955-2963

Perrem K, Bryan TM, Englezou A, Hackl T, Moy EL & Reddel RR (1999) Repression of an alternative mechanism for lengthening of telomeres in somatic cell hybrids. *Oncogene* 18: 3383–3390

Perrem K, Colgin LM, Neumann AA, Yeager TR & Reddel RR (2001) Coexistence of alternative lengthening of telomeres and telomerase in hTERT-transfected GM847 cells. *Mol Cell Biol* 21: 3862–3875

Pestana A, Vinagre J, Sobrinho-Simões M & Soares P (2017) TERT biology and function in cancer: beyond immortalisation. *J Mol Endocrinol* 58: R129–R146

Roake CM & Artandi SE (2020) Regulation of human telomerase in homeostasis and disease. *Nat Rev Mol Cell Biol* 21: 384–397

Root H, Larsen A, Komosa M, Al-Azri F, Li R, Bazett-Jones DP & Meyn MS (2016) FANCD2 limits BLM-dependent telomere instability in the alternative lengthening of telomeres pathway. *Hum Mol Genet* 25: 3255–3268

Sfeir A, Kosiyatrakul ST, Hockemeyer D, MacRae SL, Karlseder J, Schildkraut CL & de Lange T (2009) Mammalian telomeres resemble fragile sites and require TRF1 for efficient replication. *Cell* 138: 90–103

Sfeir A & De Lange T (2012) Removal of shelterin reveals the telomere end-protection problem. *Science* 336: 593–597

Shay JW & Bacchetti S (1997) A survey of telomerase activity in human cancer. *Eur J Cancer* 33: 787–791

Shay JW & Wright WE (2005) Senescence and immortalization: role of telomeres and telomerase. *Carcinogenesis* 26: 867–874

Silva B, Pentz R, Figueira AM, Arora R, Lee YW, Hodson C, Wischnewski H, Deans AJ & Azzalin CM (2019) FANCM limits ALT activity by restricting telomeric replication stress induced by deregulated BLM and R-loops. *Nat Commun* 10: 2253

Sobinoff AP & Pickett HA (2017) Alternative lengthening of telomeres: DNA repair pathways converge. *Trends Genet* 33: 921–932

Sobinoff AP & Pickett HA (2020) Mechanisms that drive telomere maintenance and recombination in human cancers. *Curr Opin Genet Dev* 60: 25–30

Sui J, Lin Y-F, Xu K, Lee K-J, Wang D & Chen BPC (2015) DNA-PKcs phosphorylates hnRNP-A1 to facilitate the RPA-to-POT1 switch and telomere capping after replication. *Nucleic Acids Res* 43:5971-5983

Takakura M, Kyo S, Kanaya T, Tanaka M & Inoue M (1998) Expression of human telomerase subunits and correlation with telomerase activity in cervical cancer. *Cancer Res* 58:1558-1561

Teng SC, Chang J, McCowan B & Zakian VA (2000) Telomerase-independent lengthening of yeast telomeres occurs by an abrupt Rad50-dependent, Rif-inhibited recombinational process. *Mol Cell* 6: 947–952

Tilman G, Loriot A, Van Beneden A, Arnoult N, Londõno-Vallejo JA, De Smet C & Decottignies A (2009) Subtelomeric DNA hypomethylation is not required for telomeric sister chromatid exchanges in ALT cells. *Oncogene* 28: 1682–1693

Ting NSY, Yu Y, Pohorelic B, Lees-Miller SP & Beattie TL (2005) Human Ku70/80 interacts directly with hTR, the RNA component of human telomerase. *Nucleic Acids Res* 33: 2090-2098

Ting NSY, Pohorelic B, Yu Y, Lees-Miller SP & Beattie TL (2009) The human telomerase RNA component, hTR, activates the DNA-dependent protein kinase to phosphorylate heterogeneous nuclear ribonucleoprotein A1. *Nucleic Acids Res* 37: 6105-6115

Toledo LI, Altmeyer M, Rask MB, Lukas C, Larsen DH, Povlsen LK, Bekker-Jensen S, Mailand N, Bartek J & Lukas J (2013) ATR prohibits replication catastrophe by preventing global exhaustion of RPA. *Cell* 155: 1088-1103

Tseng CK, Wang HF, Burns AMM, Schroeder MRR, Gaspari M & Baumann P (2015) Human telomerase RNA processing and quality control. *Cell Rep* 13: 2232–2243

Verdun RE & Karlseder J (2006) The DNA damage machinery and homologous recombination pathway act consecutively to protect human telomeres. *Cell* 127: 709–720

Viceconte N, Dheur MS, Majerova E, Pierreux CE, Baurain JF, van Baren N & Decottignies A (2017) Highly aggressive metastatic melanoma cells unable to maintain telomere length. *Cell Rep* 19: 2529–2543

Vulliamy T, Beswick R, Kirwan M, Marrone A, Digweed M, Walne A & Dokal I (2008) Mutations in the telomerase component NHP2 cause the premature ageing syndrome dyskeratosis congenita. *Proc Natl Acad Sci USA* 105: 8073–8078

Wang C & Meier UT (2004) Architecture and assembly of mammalian H/ACA small nucleolar and telomerase ribonucleoproteins. *EMBO J* 23: 1857–1867

Yang S-H & Sharrocks AD (2005) PIASx acts as an Elk-1 coactivator by facilitating derepression. *EMBO J.* 24**:** 2161–2171

Yeager TR, Neumann AA, Englezou A, Huschtscha LI, Noble JR & Reddel RR (1999) Telomerase-negative immortalized human cells contain a novel type of promyelocytic leukemia (PML) body. *Cancer Res* 59: 4175–4179

Yuan X, Larsson C & Xu D (2019) Mechanisms underlying the activation of TERT transcription and telomerase activity in human cancer: old actors and new players. *Oncogene* 38: 6172–6183

Zhang JM, Yadav T, Ouyang J, Lan L & Zou L (2019a) Alternative lengthening of telomeres through two distinct break-induced replication pathways. *Cell Rep* 26: 955-968.e3

Zhang T, Zhang Z, Shengzhao G, Li X, Liu H & Zhao Y (2019b) Strand break-induced replication fork collapse leads to C-circles, C-overhangs and telomeric recombination. *PLoS Genet* 15: e1007925

Zhao J, Bilsland A, Jackson K & Keith WN (2005) MDM2 negatively regulates the human telomerase RNA gene promoter. *BMC Cancer* 5:6

Figure Legends

Figure 1. Repression of telomerase activity in ALT$^+$ hybrids and progressive silencing of h*TR* gene in SI24/ALT$^+$ cells.

A. Left: Telomerase activity measured using ddTRAP assay. The horizontal pink lines represent the threshold used in these samples for background correction. Each dot on the ddPCR output represents a unique droplet that is either positive or negative for fluorescent signal. Right: Quantification of TRAP activity after normalization to SW39/TEL$^+$ cells (n=3).

B. *hTR* and *hTERT* expression, normalized to *ACTB* mRNA and to SW39/TEL$^+$.

C. RNA Pol II binding at h*TR* promoter in SI14/TEL$^+$, SI24/ALT$^+$ and 8G12/ALT$^+$ cell lines, normalized to H3 ChIP. Control loci with, respectively, high or low transcriptional activity: *c-fos* promoter and subtelomeric *4qHox* locus (n=3). Statistical analyses were performed using one-way ANOVA with post-hoc Tukey's test for multiple comparisons.

D. H3K9me3 and H3K27me3 (left) or H3K4me3 and H3Ac (right) densities at h*TR* promoter in SI14/TEL$^+$ and SI24/ALT$^+$, normalized to H3 (n=3). Control loci as in C.

E. NFYB binding at h*TR* promoter in SI14/TEL$^+$, SI24/ALT$^+$, SW39/TEL$^+$ and IMRB/ALT$^+$ cells normalized to H3. Control loci with, respectively, high and low NFYB binding: *hnRNPA1* promoter and subtelomeric *4qHox* (n=3).

Data are presented as mean ± SD. Statistical analyses were performed with Student's two-tailed unpaired t-test with Welch's correction for normality of distribution unless specified otherwise. PTM, post-translational modification.

Figure 2. NHP2 protein levels are downregulated in 8G12/ALT$^+$ cells and ectopic NHP2 overexpression silences h*TR*.

A. Western blot for h*TR* chaperone proteins in TEL$^+$ and ALT$^+$ hybrids. β-Actin is used as loading control. Quantification of western blots is shown on the right, normalized to β-Actin and to SI14/TEL$^+$ cells (n=2-4). Statistical analyses were performed using one-way ANOVA with post-hoc Tukey's test for multiple comparisons.

B. *NHP2* mRNA expression levels, normalized to *ACTB* mRNA and to SI14/TEL$^+$ cells (n=3).

C. Western blot for NHP2 in SI14/TEL$^+$, SI24/ALT$^+$ and 8G12/ALT$^+$ cell lines treated with DMSO or 10 μM MG132 for 6 h. β-Actin served as loading control. Quantifications are shown on the right, normalized to β-Actin and to SI14/TEL$^+$ cells (n=5). Statistical analyses were performed with Student's two-tailed unpaired t-test.

D. h*TR* RNA and *NHP2* mRNA expression, normalized to *ACTB* mRNA and to SI14/TEL$^+$.

E. Telomerase activity measured with ddTRAP assay in NHP2-overexpressing 8G12/ALT$^+$cells, normalized to NHP2-overexpressing SI14/TEL$^+$.

F. (Top) Western blot for NHP2 overexpression in 8G12/ALT$^+$ clonal cell lines. β-Actin served as loading control. SI14/TEL$^+$ cells are shown as reference for NHP2 expression in hybrids. (Bottom) Western blot for NHP2 overexpression in SI14/TEL$^+$ and 8G12/ALT$^+$ cells compared to empty vector control. β-Actin served as loading control.

G. h*TR* RNA*, hTERT* and *NHP2* mRNA expression, normalized to *ACTB* mRNA and to SI14/TEL$^+$ (n=3).

H. RNA Pol II binding at h*TR* promoter, normalized to H3 ChIP (n=3). See Fig. 1C legend for control loci. Statistical analyses were performed using one-way ANOVA with post-hoc Tukey's test for multiple comparisons.

Data are presented as mean ± SD.

Figure 3. h*TR*-expressing ALT$^+$ cell lines display reduced NHP2 protein levels.

A. h*TR* RNA*, hTERT* and *NHP2* mRNA expression, normalized to *ACTB* mRNA and to 143B/TEL$^+$ cells, in a series of TEL$^+$ and ALT$^+$ human cell lines as indicated (n=3).

B. Western blot for NHP2 expression. β-Actin served as loading control. Quantification is shown on the right after normalization to β-Actin and to 143B/TEL$^+$ cells (n=3).

Data are presented as mean ± SD. Statistical analyses were performed using one-way ANOVA with post-hoc Tukey's test for multiple comparisons.

Figure 4. Ectopic expression of h*TR* in ALT$^+$/hTR$^-$/hTERT$^-$ cells downregulates p-RPA32^{S33} abundance at telomeres.

A. *hTR* RNA expression, normalized to *ACTB* mRNA and to U2OS cells (n=3).

B. Western blot for NHP2 expression in the early passages of h*TR*-expressing IMRB or U2OS cells, with β-Actin as loading control.

C. Quantification of doubling time for U2OS, U2OS-hTR, IMRB and IMRB-hTR cell lines (n=3). Statistical analyses were performed with Student's two-tailed unpaired t-test with Welch's correction for normality of distribution

D. Western blot in U2OS and U2OS-hTR cells treated with or without Hydroxyurea (2 mM for 24 h), for the indicated proteins. β-Actin and Vinculin served as loading controls.

E. Representative images for co-localization between p-RPA32^{S33} (green) and telomeres (red FISH probe). White arrows indicate co-localization events. Scale bars: 5 μm. Quantification is

shown on the right. At least 50 nuclei were scored in each of the three independent experiments performed. Each dot represents the number of p-RPA32^{S33}-telomere co-localizations in one nucleus. Statistical analyses were performed with Student's two-tailed unpaired t-test with Welch's correction for normality of distribution.

F. Quantification of live cell numbers with trypan blue staining and manual counting, 72 h post-transfection with siLuc, sihTR$^{\#1}$ or sihTR$^{\#2}$, measured as the percentage of siLuc-treated cells (n=3). On the right, representative images of U2OS cells treated with sihTR$^{\#1}$ for 72 h. Statistical analyses were performed using one-way ANOVA with post-hoc Tukey's test for multiple comparisons.

G. Western blot analyses in the indicated cell lines cells transfected for 48 h with siLuc or sihTR, with the indicated antibodies. U2OS cells treated with Hydroxyurea (2 mM for 24 h) were used as positive controls.

Data are shown as mean ± SD, with the red line marking the mean value.

Figure 5. Ectopic expression of h*TR* in ALT$^+$/hTR$^-$/hTERT$^-$ cells exacerbates telomeric damages and C-circle formation.

A. Representative images for fragile telomeres using the CO-FISH assay. Lagging strands (C-probe) and leading strands (G-probe) were marked with green PNA probes and red LNA probes, respectively. White circles and arrows indicate "smeary" or "doublet" telomeric signals, respectively. Quantification of fragile telomeres is shown on the right as the percentage of total telomeres counted (n=932-1073). Comparison of fragile to non-fragile telomere percentage was performed using X^2-test.

B. Representative images for co-localization between RAD51 (green) and telomeres (red FISH probe). White arrows indicate representative RAD51-telomere co-localization events. Quantifications are shown on the right. A total of 120 nuclei were scored from two independent experiments.

C. Representative images for TIF quantification: co-localization between 53BP1 (green) and telomeres (red FISH probe) in U2OS or IMRB cells with or without ectopic h*TR* overexpression. White arrows indicate TIF. Quantification of TIF is on the right. A total of 110-170 nuclei were scored from three independent experiments. Each dot represents the number of TIF per nucleus.

D. Representative images for TIF quantification, as in (A), in U2OS or U2OS-hTR cells, treated as indicated with DMSO or 5 μM ATRi or 5 μM ATMi for 20 h. White arrows indicate TIF.

E. Quantification of TIF from (D). At least 65 nuclei were scored in each of the two independent experiments performed. Each dot represents the number of TIF per nucleus. Statistical analyses were performed using one-way ANOVA with post-hoc Games-Howell's test for multiple comparisons.

F. Representative images for co-localization between POLD3 (red) and RAP1 (green). White arrows indicate co-localization events. Quantification of co-localization events between POLD3 and RAP1 is shown on the right. A total of 190-230 nuclei were scored from three independent experiments.

G. C-circle analysis using slot-blot assay hybridized with radioactive C-rich telomeric probe. Quantification is shown below (n=7). Statistical analyses were performed using the non-parametrical Mann Whitney test.

H,I. C-circle analyses in the indicated cell lines 72 h after treatment with siPOLD3 or siLuc used as control for transfection. Quantifications are shown below (n=3). siSMARCAL1 was used as positive control for increased C-circle production in cells with defective fork reversal activity (Zhang *et al*, 2019b).

All scale bars: 5 μm. Data are shown as mean ± SD. B, C, E and F: the red line marks the mean value. Statistical analyses were performed with Student's two-tailed unpaired t-tests with Welch's correction for normality of distribution, unless specified otherwise.

Figure 6. More APBs are actively engaged in G2/M telomeric DNA synthesis in ALT$^+$ cells ectopically expressing h*TR*.

A. Representative images for co-localization between PML (green) and telomeres (red FISH probe). White arrows indicate co-localization events, marking APBs. Quantification of images is shown on the right. A total of 85-300 nuclei were scored from four independent experiments. Each dot represents the number of events per nucleus: PML foci or APBs.

B. Experimental scheme for ATSA (ALT telomere DNA synthesis in APBs), used to measure G2/M telomeric DNA synthesis, within PML bodies.

C. Representative images for co-localization between EdU (green) and telomeres (red FISH probe) within PML bodies (cyan) in U2OS and U2OS-hTR cells. White arrows indicate co-localization events.

D, E. Quantification of images shown in (C). Co-localization events between EdU foci and APBs were analyzed (D) and the percentage of APBs that are actively engaged in G2/M telomeric synthesis was calculated (E). A total of at least 50 nuclei were scored from three independent experiments.

All scale bars: 5 μm. Data are shown as mean ± SD, with the red line marking the mean value. Statistical analyses were performed with Student's two-tailed unpaired t-test with Welch's correction for normality of distribution.

Figure 7. h*TR* overexpression induces a DNA-PK and hnRNPA1-dependent depletion of RPA from ALT telomeres.

A. Representative images for co-localization between RPA32 (green) and single stranded C-rich telomeric sequences (ss-Telo-C, red FISH probe), in G2/M-synchronized cells. White arrows indicate co-localization events.

B. Quantification of images in (A). A total of at least 55 nuclei were scored from three independent experiments. Each dot represents the number of events per nucleus.

C. Quantification of images in (A) as the percentage of single stranded C-rich telomeric sequences associated with RPA32 to total single stranded C-rich telomeric sequences A total of at least 55 nuclei were scored from three independent experiments.

D. Representative images for co-localization between RPA32 or p-RPA32^{S33} (green) and telomeres (red FISH probe), in the indicated cell lines treated with siLuc or sihnRNPA1 for 48 h. White arrows indicate co-localization events.

E. Quantification of images in (D). A total of 85-135 nuclei were scored from three independent experiments. Each dot represents the number of events per nucleus. Statistical analyses were performed using one-way ANOVA with post-hoc Games-Howell's test for multiple comparisons.

F. Representative images for co-localization between RPA32 (green) and telomeres (red FISH probe) in the indicated cell lines treated with either DMSO or 10 μM NU7026 DNA-PK-inhibitor (DNA-PK-i) for 48 h. White arrows indicate co-localization events. Quantifications are shown on the right. A total of 53-84 nuclei were scored from three independent experiments. Statistical analyses were performed using one-way ANOVA with post-hoc Games-Howell's test for multiple comparisons.

All scale bars: 5 μm. Data are shown as mean ± SD, with the red line marking the mean value. Statistical analyses were performed with Student's two-tailed unpaired t-test with Welch's correction for normality of distribution unless specified otherwise.

Figure 8. NHP2 regulates 53BP1 recruitment at damaged telomeres and IR-induced DSBs.

A. h*TR* and *NHP2* mRNA expression in U2OS-hTR cells 72 h post-transfection with siLuc or siNHP2, normalized to *ACTB* mRNA and to SI14/TEL^{+} cells (n=2).

B. Western blot showing NHP2 protein levels in the indicated cells treated with siLuc or siNHP2, 72 h post-transfection. β-Actin served as loading control.
C. Representative images for co-localization between p-RPA32^{S33} (green) and telomeres (red FISH probe) in U2OS-hTR cells treated with control siLuc or siNHP2, 72 h post-transfection. White arrows indicate co-localization events. Quantification of images is shown on the right. Each dot indicates the number of co-localization events per nucleus (n=2). Statistical analyses were performed with Student's two-tailed unpaired t-tests with Welch's correction for normality of distribution.

D. Representative images for TIF quantification: co-localization between 53BP1 (green) and telomeres (red FISH probe), measured 72 h post-transfection with siLuc or siNHP2 in cells further treated with either DMSO or Doxorubicin (DOXO, 1.5 μM) for 2 h. White arrows indicate TIF. Quantification of TIF is shown on the right. A total of at least 100 nuclei were scored from two independent experiments. Each dot represents the number of TIF per nucleus. Statistical analyses were performed using one-way ANOVA with post-hoc Games-Howell's test for multiple comparisons.
E. Western blot analyses in U2OS and U2OS-hTR cells treated with the indicated siRNAs, 72 h post-transfection to detect total protein levels using the indicated antibodies. β-Actin and Vinculin served as loading controls.
F. Representative images for 53BP1 foci formation in U2OS and U2OS-hTR cells, 72 h post-transfection with siLuc or siNHP2, exposed to 1 Gy irradiation and fixed at various time points post-irradiation as indicated.
G. Quantification of images shown in (F). Each dot represents the number of 53BP1 foci per nucleus. A total of 114-140 nuclei were scored from two independent experiments. Statistical analyses were performed using two-way ANOVA Mixed effect model.
All scale bars: 5 μm. Data are shown as mean ± SD, with the red line marking the mean value.

Figure 9. Hypothetical model for the regulation of ALT telomere homeostasis by h*TR* and NHP2.

In TEL^{+} cells, h*TR,* along with its chaperone proteins including NHP2, associates with hTERT to form the functional telomerase holoenzyme complex. At ALT telomeres, ATR kinase activity mitigates recovery of stalled replication forks via fork regression and repair. Likely through its previously reported interaction with KU subunits, h*TR* expression in ALT^{+}/hTR^{-} cells induces the removal of RPA from telomeres by the DNA-PK/hnRNPA1 complex. The reduced RPA/p-

RPA^{S33} abundance at ALT telomeres, in turn, reduces RAD51 recruitment and increases replication fork collapse events. These collapsed forks provide the substrate for break-induced telomere synthesis that concomitantly leads to POLD3-dependent C-circle production. If left unrepaired, collapsed forks can be further marked by 53BP1 in a process regulated by NHP2. Finally, h*TR* has a second important non-canonical, anti-apoptotic function as previously described (Gazzaniga & Blackburn, 2014), in both TEL^+ and ALT^+ cell lines.

Supplementary figures

Figure S1. Knockdown of NHP2 in TEL^+ cells abrogates telomerase activity but NHP2 overexpression does not rescue telomerase activity in 8G12/ALT^+ cells.

A. *hTR* RNA and *NHP2* mRNA expression in SI14/TEL^+ and 6C3/TEL^+ cells, 72 h post siLuc- or siNHP2-transfection, normalized to *ACTB* mRNA and to respective siLuc cells.

B. Telomerase activity measured with ddTRAP assay in SI14/TEL^+ and 6C3/TEL^+ cells, 72 h post siLuc- or siNHP2- transfection, normalized to SI14/TEL^+ siLuc. See Fig. 1A legend for details.

C. Telomerase activity measured with ddTRAP assay in NHP2-overexpressing 8G12/ALT^+ stable clonal cell lines, normalized to SI14/TEL^+ (n=3).

Figure S2. Characterization of TEL^+ and ALT^+ human cell lines.

LB23/TEL^+ and LB188/ALT^+ cell lines were established from rhabdomyosarcoma tumors. LB857/ALT^+ cell line derives from a myxoid sarcoma tumor. All three cell lines were established in-house.

A. Quantification of telomerase activity using ddTRAP assay after normalization to LB23/TEL^+ cells (n=3).

B. C-circle analysis using slot-blot assay, hybridized with a radioactive C-rich telomeric probe. Quantification is shown below and compared to U2OS/ALT^+ cells. Data are shown as mean ± SD (n=2).

C. TRF using *Hinf*I/*Rsa*I restriction enzymes in the indicated cell lines.

D. Representative images for co-localization between PML (green) and telomeres (red FISH probe). White arrows indicate APBs. Quantification is shown on the right. Each dot represents the number of APBs per nucleus. Scale bar: 5 μm.

Figure S3. Characterization of IMRB-hTR^{late} cells and telomere length in U2OS-hTR and IMRB-hTR cells.

A. Western blot for NHP2 expression in the indicated cell lines with β-Actin as loading control. IMRB-hTR^{late} cells refer to late passage IMRB-hTR cells that set up adaptive mechanisms.

B. h*TR* RNA or *NHP2* mRNA expression in the indicated cell lines, normalized to *ACTB mRNA* and to IMRB cells (n=3).

C. Dot-blot to detect relative telomere length in U2OS-hTR and IMRB-hTR cell lines, probed with γ-^{32}P labelled telomeric C-rich probe (n=4). Quantifications are shown on the right with normalization to the respective parental cell lines. Statistical analyses were performed using Student's two-tailed unpaired t-tests with Welch's correction for normality of distribution.

Figure S4. p-RPA32^{S33} levels in TEL^{+} and ALT^{+} cells.

A. Representative images for co-localization between p-RPA32^{S33} (green) and telomeres (red FISH probe) in U2OS cells treated with DMSO or 5 μM VE-821 ATRi. Quantification is shown on the right. A total of at least 150 nuclei were scored from three independent experiments. Each dot represents the number of p-RPA32^{S33}-telomere co-localizations per nucleus. All scale bars: 5 μm. Data are shown as mean ± SD, with the red line marking the mean value. Statistical analysis was performed using Student's two-tailed unpaired t-tests with Welch's correction for normality of distribution.

B. Western blot analysis for detecting p-RPA32^{S33} and RPA32 levels in the indicated cell lines, under unperturbed conditions. β-Actin served as loading control.

Figure S5. ATR knock-down reduces C-circle abundance in U2OS-hTR cells.

C-circle analysis in the U2OS and U2OS-hTR cells 72 h after transfection with siLuc or siATR, normalized to U2OS siLuc. Quantifications are shown on the right relative to U2OS siLuc (n=4-5).

Statistical analyses were performed using one-way ANOVA with post-hoc Tukey's test for multiple comparisons

Figure S6. *PML* mRNA expression in U2OS, U2OS-hTR, IMRB and IMRB-hTR cells.

PML mRNA expression in U2OS-hTR and IMRB-hTR cell lines, normalized to *ACTB* mRNA and to the respective parental cell lines**.**

Figure S7. Increased single stranded G-rich telomeric DNA in U2OS-hTR cells and *hnRNPA1* knock-down efficiency.

A. Representative images for single stranded G-rich telomeric sequences (green FISH probe), in cells synchronized in G2/M phase. Quantification of images is shown on the right. A total of at least 50 nuclei were scored from two independent experiments. Statistical analysis was performed using Student's two-tailed unpaired t-tests.

B. *hnRNPA1* mRNA levels in the indicated cell lines normalized to *ACTB* and respective siLuc-treated cells (n=2).

Figure S8. NHP2 regulates 53BP1 signaling.

A. Quantification of images in Fig 8D for total 53BP1 foci and non-telomeric 53BP1 foci in the indicated cell lines and conditions. A total of at least 90 nuclei were scored from two independent experiments. Statistical analysis was performed using one-way ANOVA with post-hoc Games-Howell's test for multiple comparisons.

B. Representative images for TIF quantification: co-localization between 53BP1 (green) and telomeres (red FISH probe), measured 72 h post-transfection with siLuc or siNHP2 in SaOS-2/ALT$^+$ cells. Quantification is shown on the right. A total of at least 75 nuclei were scored from two independent experiments.

C. Representative images for TIF quantification: co-localization between 53BP1 (green) and telomeres (red FISH probe), measured 72 h post-transfection with siLuc or siNHP2 in 143B/TEL$^+$ cells further treated with either DMSO or Doxorubicin (DOXO, 1.5 μM) for 2 h. White arrows indicate TIF.

D,E. Quantification of 53BP1 foci and TIF, respectively from (C). A total of at least 75 nuclei were scored from two independent experiments. Each dot represents the number of 53BP1 or TIF per nucleus.

All scale bars: 5 μm. Data are shown as mean ± SD, with the red line marking the mean value. Statistical analysis was performed using Student's two-tailed unpaired t-tests with Welch's correction for normality of distribution, unless specified otherwise.

Figure S9. NHP2 regulates γH2AX foci formation in irradiated cells.

A. Representative images for γH2AX foci formation in U2OS and U2OS-hTR cells, 72 h post-transfection with siLuc or siNHP2, exposed to 1 Gy irradiation and fixed at various time points post-irradiation as indicated.

B. Quantification of images shown in (A). A total of 35-75 nuclei were scored. Each dot represents the number of γH2AX foci per nucleus at the indicated time points of recovery.

All scale bars: 5 μm. Data are shown as mean ± SD, with the red line marking the mean value.

Figure 1

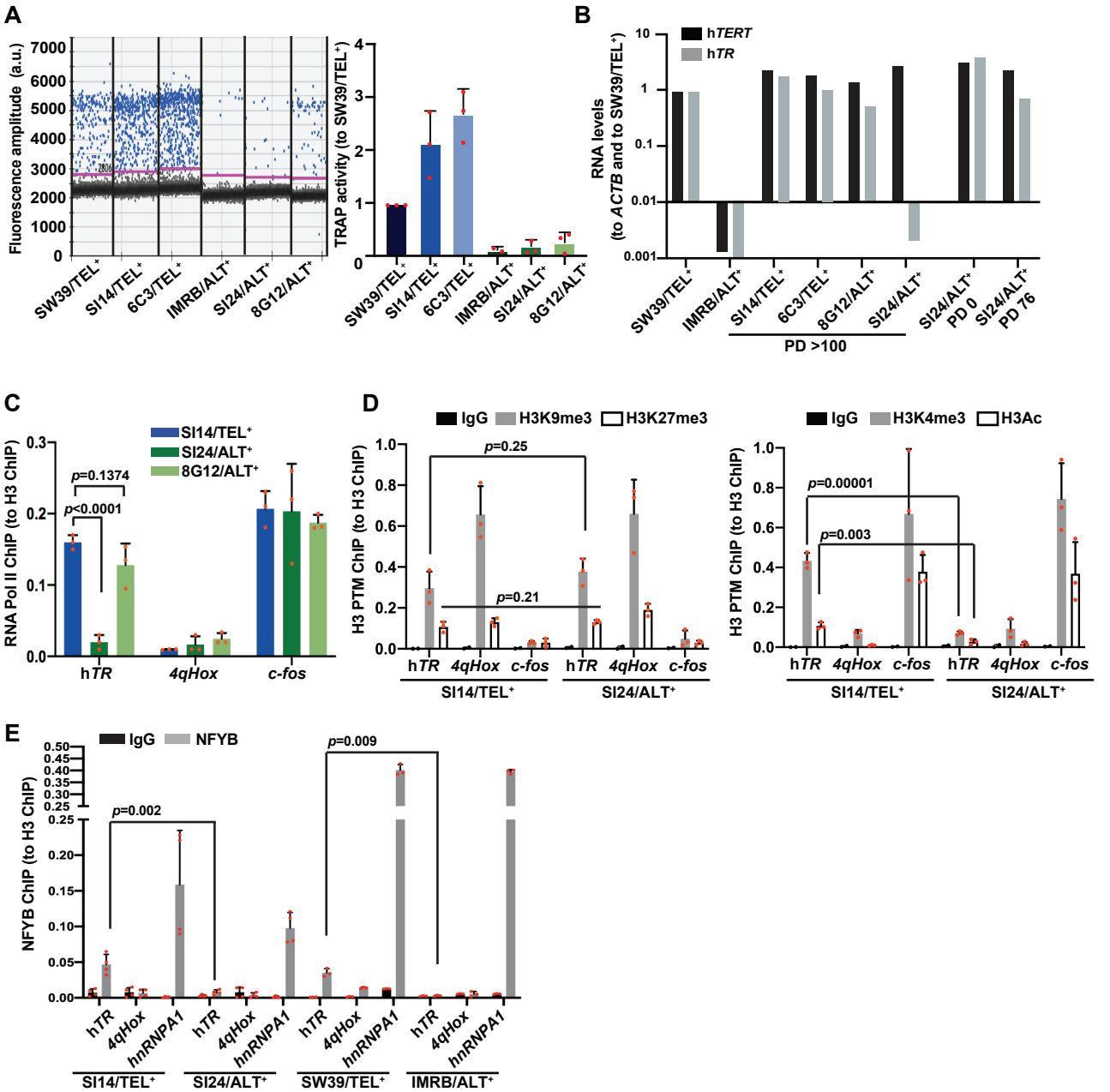
A
Fluorescence amplitude (a.u.)
TRAP activity (to SW39/TEL+)
SW39/TEL+
SI14/TEL+
6C3/TEL+
IMRB/ALT+
SI24/ALT+
8G12/ALT+
B
hTERT
hTR
RNA levels (to ACTB and to SW39/TEL+)
PD >100
SI24/ALT+ PD 0
SI24/ALT+ PD 76
C
RNA Pol II ChIP (to H3 ChIP)
p=0.1374
p<0.0001
hTR
4qHox
c-fos
D
IgG
H3K9me3
H3K27me3
H3K4me3
H3Ac
H3 PTM ChIP (to H3 ChIP)
p=0.25
p=0.21
p=0.00001
p=0.003
E
NFYB
NFYB ChIP (to H3 ChIP)
p=0.002
p=0.009
hnRNPA1

Figure 2

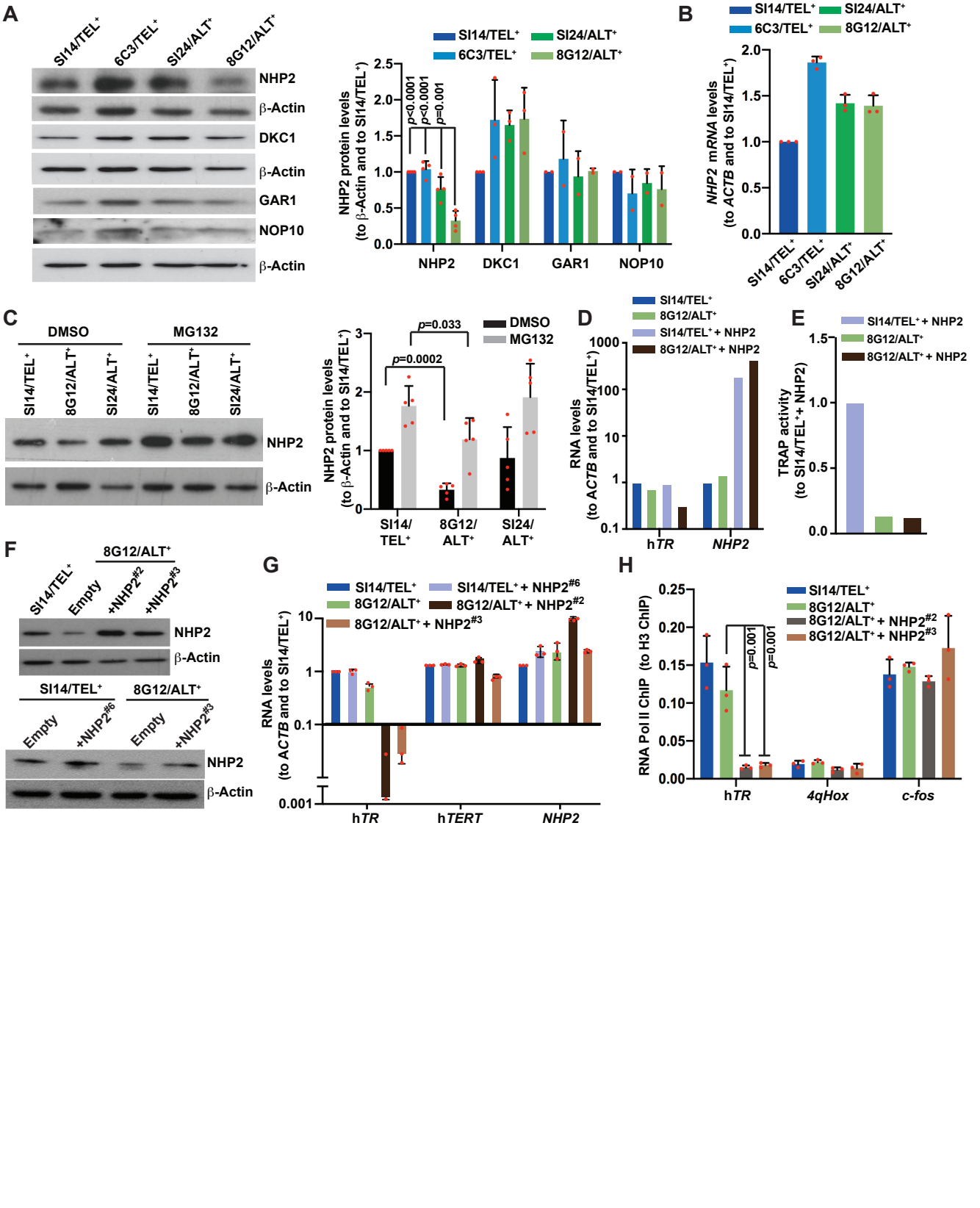
A
SI14/TEL+
6C3/TEL+
SI24/ALT+
8G12/ALT+
NHP2
β-Actin
DKC1
β-Actin
GAR1
NOP10
β-Actin
NHP2 protein levels (to β-Actin and to SI14/TEL+)
p<0.0001
p<0.0001
p=0.001
NHP2
DKC1
GAR1
NOP10
B
NHP2 mRNA levels (to ACTB and to SI14/TEL+)
C
DMSO
MG132
NHP2
β-Actin
p=0.033
p=0.0002
NHP2 protein levels (to β-Actin and to SI14/TEL+)
SI14/ TEL+
8G12/ ALT+
SI24/ ALT+
D
SI14/TEL+ + NHP2
8G12/ALT+ + NHP2
RNA levels (to ACTB and to SI14/TEL+)
hTR
NHP2
E
TRAP activity (to SI14/TEL+ + NHP2)
F
Empty
+NHP2#2
+NHP2#3
+NHP2#6
G
RNA levels (to ACTB and to SI14/TEL+)
hTR
hTERT
NHP2
H
RNA Pol II ChIP (to H3 ChIP)
p=0.001
p=0.001
hTR
4qHox
c-fos

Figure 3

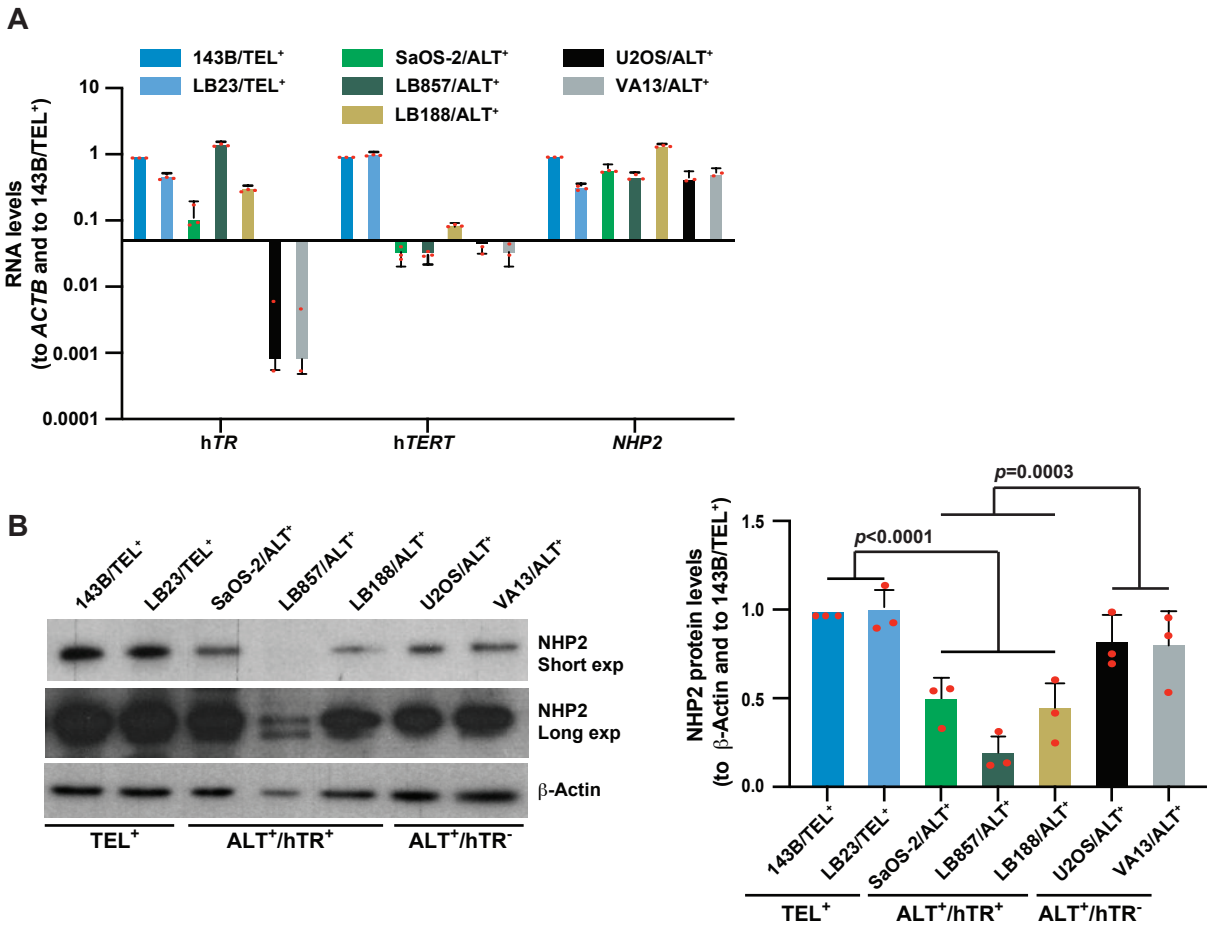
A
143B/TEL+
LB23/TEL+
SaOS-2/ALT+
LB857/ALT+
LB188/ALT+
U2OS/ALT+
VA13/ALT+
RNA levels
(to ACTB and to 143B/TEL+)
10
1
0.1
0.01
0.001
0.0001
hTR
hTERT
NHP2
B
143B/TEL+
LB23/TEL+
SaOS-2/ALT+
LB857/ALT+
LB188/ALT+
U2OS/ALT+
VA13/ALT+
NHP2
Short exp
NHP2
Long exp
β-Actin
TEL+
ALT+/hTR+
ALT+/hTR-
p=0.0003
p<0.0001
NHP2 protein levels
(to β-Actin and to 143B/TEL+)
1.5
1.0
0.5
0.0
143B/TEL+
LB23/TEL+
SaOS-2/ALT+
LB857/ALT+
LB188/ALT+
U2OS/ALT+
VA13/ALT+
TEL+
ALT+/hTR+
ALT+/hTR-

Figure 4

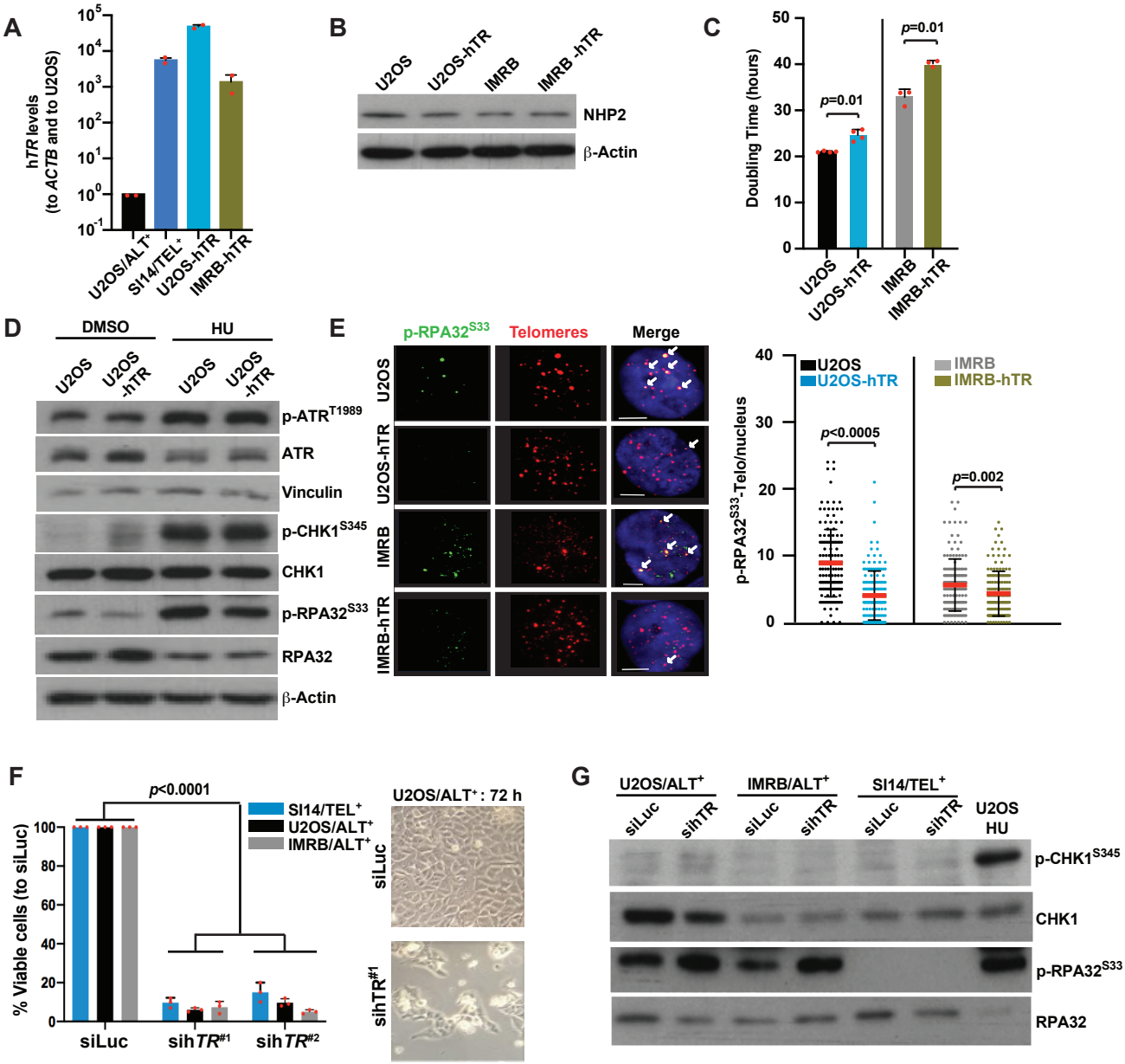
A
hTR levels (to ACTB and to U2OS)
U2OS/ALT+
SI14/TEL+
U2OS-hTR
IMRB-hTR
B
U2OS
U2OS-hTR
IMRB
IMRB-hTR
NHP2
β-Actin
C
Doubling Time (hours)
p=0.01
p=0.01
U2OS
U2OS-hTR
IMRB
IMRB-hTR
D
DMSO
HU
U2OS
U2OS -hTR
p-ATR T1989
ATR
Vinculin
p-CHK1 S345
CHK1
p-RPA32 S33
RPA32
β-Actin
E
p-RPA32 S33
Telomeres
Merge
U2OS
U2OS-hTR
IMRB
IMRB-hTR
p-RPA32 S33-Telo/nucleus
p<0.0005
p=0.002
F
p<0.0001
SI14/TEL+
U2OS/ALT+
IMRB/ALT+
% Viable cells (to siLuc)
siLuc
sihTR#1
sihTR#2
U2OS/ALT+ : 72 h
siLuc
sihTR#1
G
U2OS/ALT+
IMRB/ALT+
SI14/TEL+
siLuc
sihTR
U2OS HU
p-CHK1 S345
CHK1
p-RPA32 S33
RPA32

Figure 5

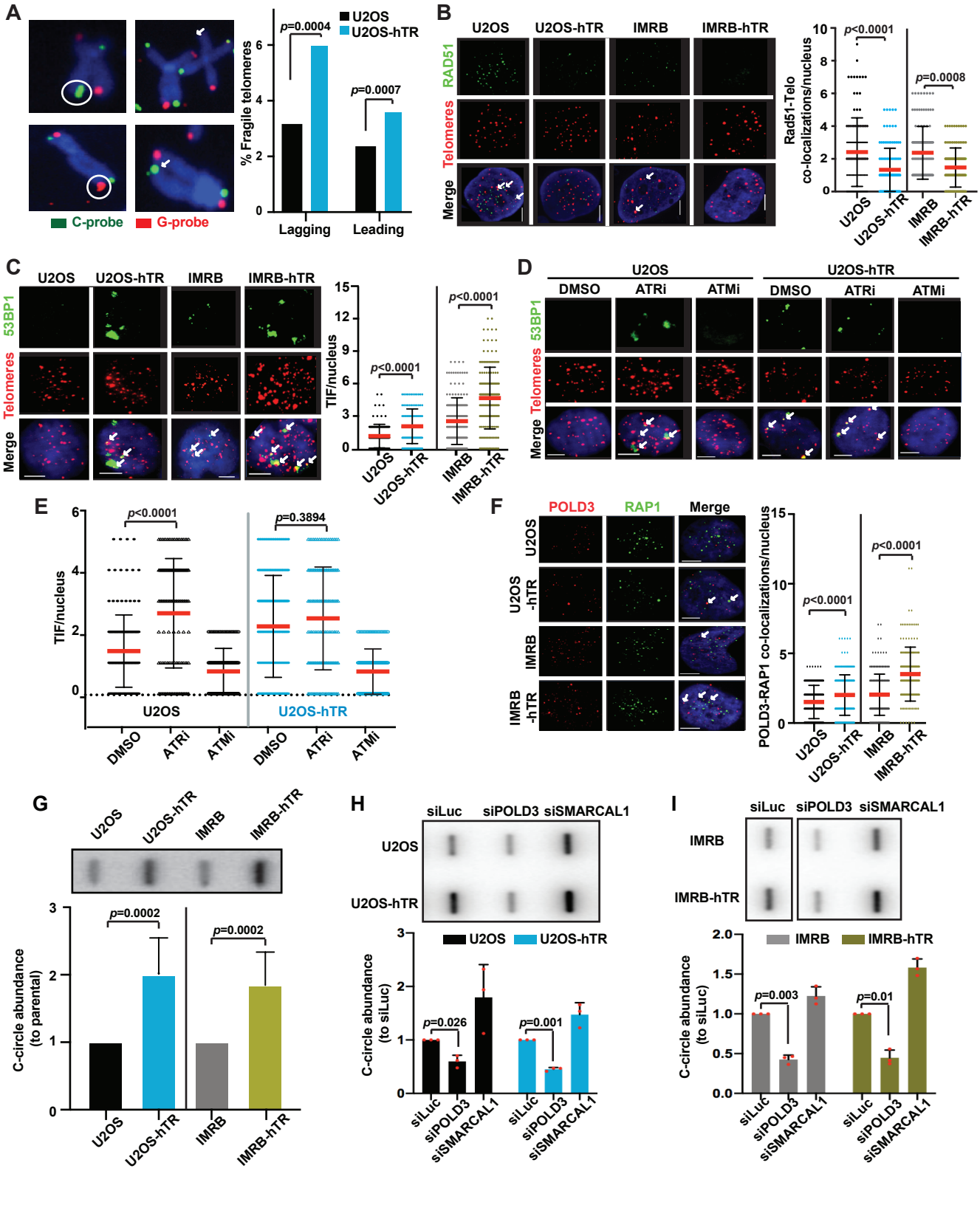
A
C-probe
G-probe
U2OS
U2OS-hTR
p=0.0004
p=0.0007
% Fragile telomeres
Lagging
Leading
B
U2OS
U2OS-hTR
IMRB
IMRB-hTR
RAD51
Telomeres
Merge
Rad51-Telo co-localizations/nucleus
p<0.0001
p=0.0008
C
53BP1
TIF/nucleus
p<0.0001
D
DMSO
ATRi
ATMi
E
p<0.0001
p=0.3894
F
POLD3
RAP1
POLD3-RAP1 co-localizations/nucleus
G
C-circle abundance (to parental)
p=0.0002
H
siLuc
siPOLD3
siSMARCAL1
C-circle abundance (to siLuc)
p=0.026
p=0.001
I
p=0.003
p=0.01

Figure 6

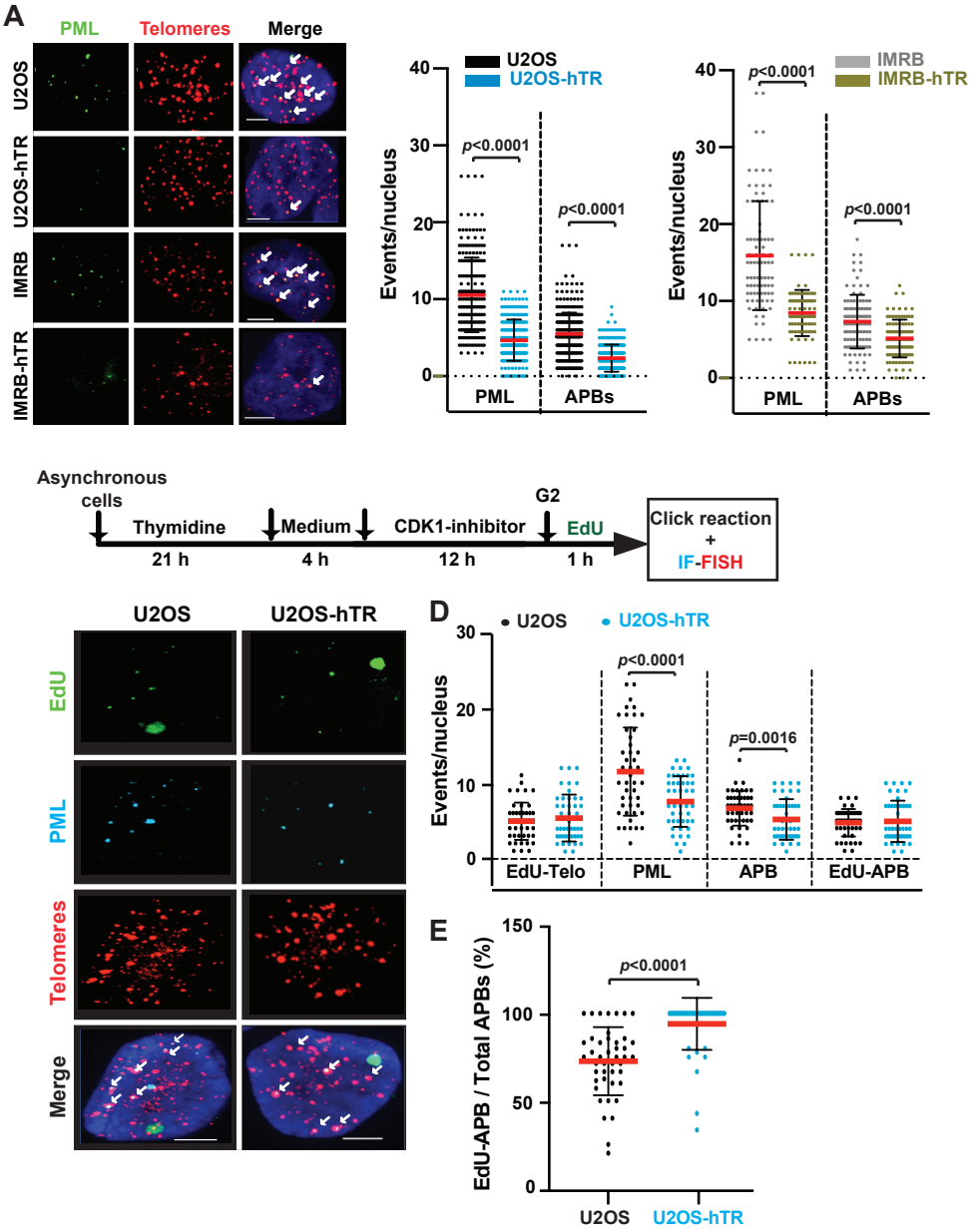
A
PML
Telomeres
Merge
U2OS
U2OS-hTR
IMRB
IMRB-hTR
Events/nucleus
p<0.0001
PML
APBs
B
Asynchronous cells
Thymidine
21 h
Medium
4 h
CDK1-inhibitor
12 h
G2
EdU
1 h
Click reaction + IF-FISH
C
EdU
PML
Telomeres
Merge
D
p=0.0016
EdU-Telo
APB
EdU-APB
E
EdU-APB / Total APBs (%)

Figure 7

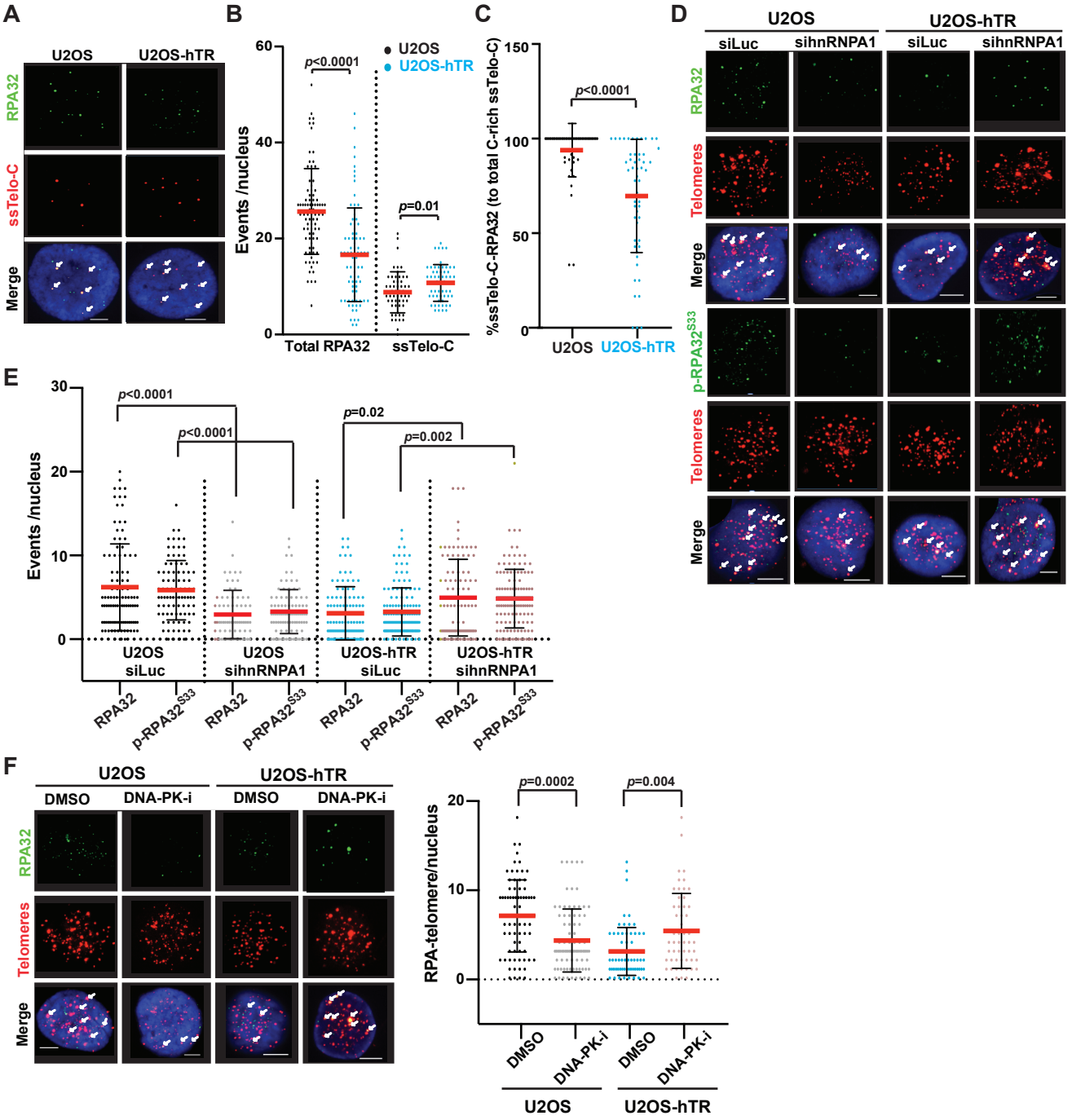
A
U2OS
U2OS-hTR
RPA32
ssTelo-C
Merge
B
U2OS
U2OS-hTR
p<0.0001
p=0.01
Events /nucleus
Total RPA32
ssTelo-C
C
p<0.0001
%ssTelo-C-RPA32 (to total C-rich ssTelo-C)
U2OS
U2OS-hTR
D
U2OS
U2OS-hTR
siLuc
sihnRNPA1
RPA32
Telomeres
Merge
p-RPA32S33
E
p<0.0001
p<0.0001
p=0.02
p=0.002
Events /nucleus
U2OS siLuc
U2OS sihnRNPA1
U2OS-hTR siLuc
U2OS-hTR sihnRNPA1
RPA32
p-RPA32S33
F
U2OS
U2OS-hTR
DMSO
DNA-PK-i
RPA32
Telomeres
Merge
p=0.0002
p=0.004
RPA-telomere/nucleus

Figure 8

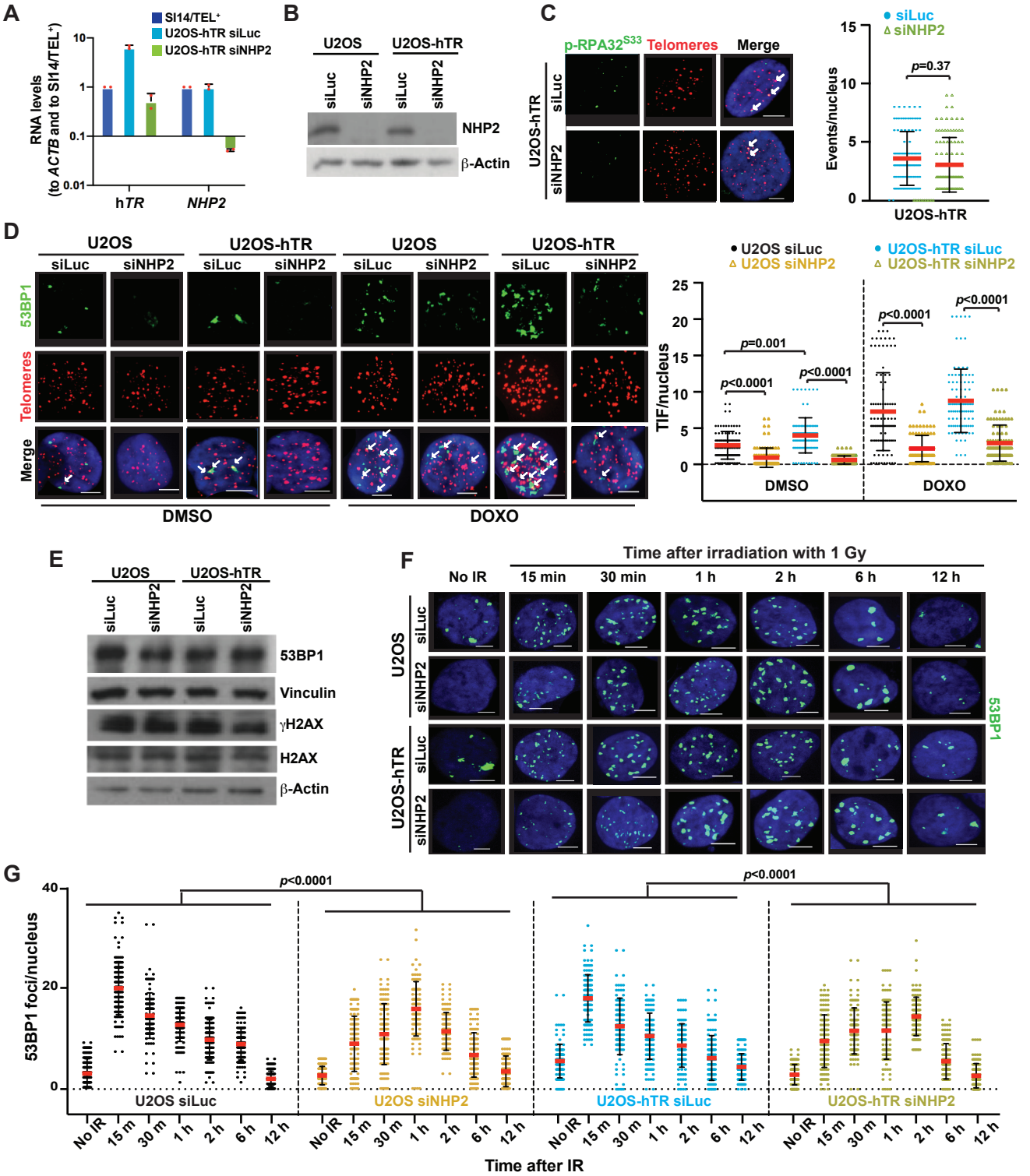
A
SI14/TEL+
U2OS-hTR siLuc
U2OS-hTR siNHP2
RNA levels (to ACTB and to SI14/TEL+)
hTR
NHP2
B
U2OS
U2OS-hTR
siLuc
siNHP2
NHP2
β-Actin
C
p-RPA32S33
Telomeres
Merge
U2OS-hTR
siLuc
siNHP2
Events/nucleus
p=0.37
D
53BP1
Telomeres
Merge
DMSO
DOXO
TIF/nucleus
p=0.001
p<0.0001
E
U2OS
U2OS-hTR
53BP1
Vinculin
γH2AX
H2AX
β-Actin
F
Time after irradiation with 1 Gy
No IR
15 min
30 min
1 h
2 h
6 h
12 h
53BP1
G
53BP1 foci/nucleus
p<0.0001
U2OS siLuc
U2OS siNHP2
U2OS-hTR siLuc
U2OS-hTR siNHP2
Time after IR

Figure 9

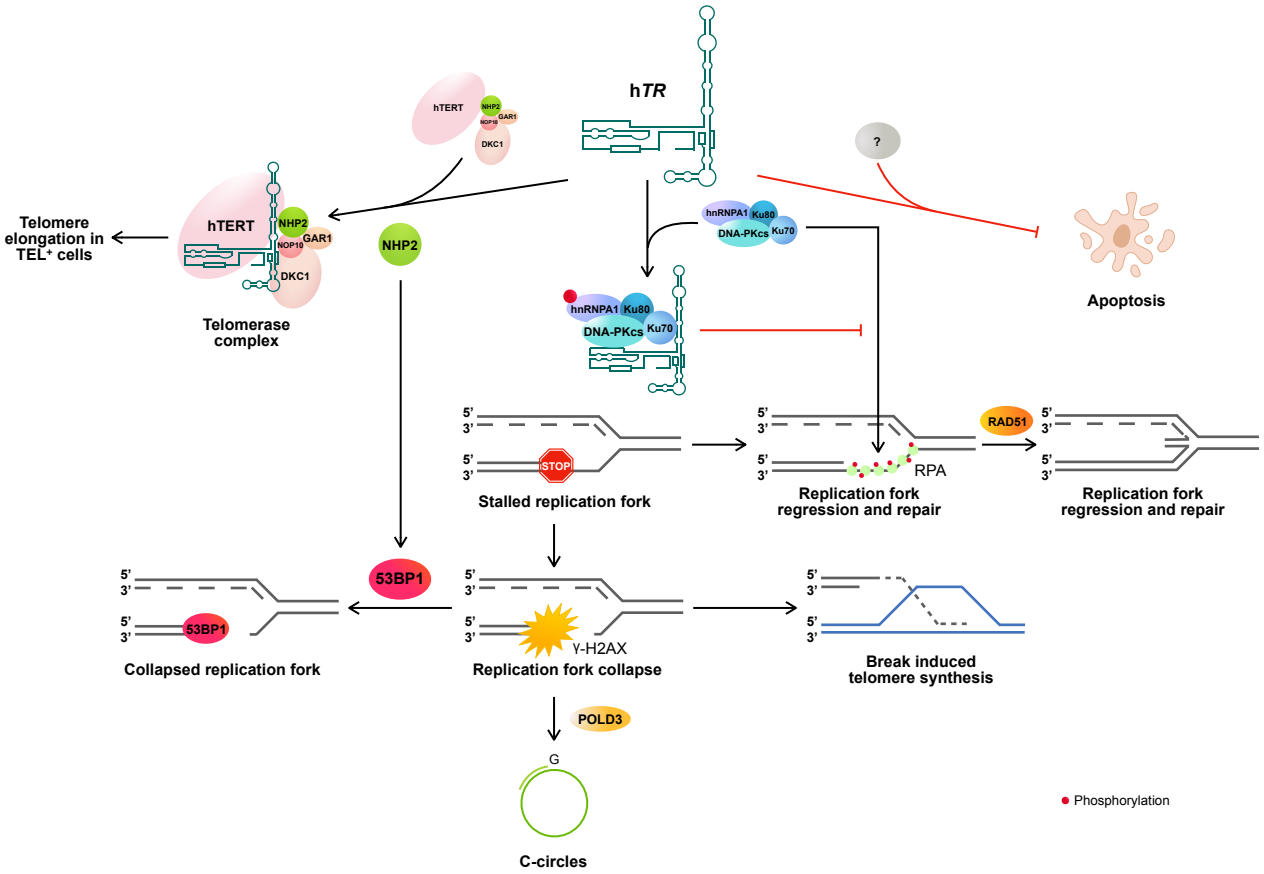
hTR
hTERT
NHP2
GAR1
NOP10
DKC1
?
Telomere elongation in TEL+ cells
Telomerase complex
hnRNPA1
Ku80
DNA-PKcs
Ku70
Apoptosis
Stalled replication fork
STOP
RPA
RAD51
Replication fork regression and repair
Replication fork regression and repair
53BP1
Collapsed replication fork
γ-H2AX
Replication fork collapse
Break induced telomere synthesis
POLD3
G
C-circles
Phosphorylation